A CDGFN-Based Quantum Multisource Information Fusion With Its Application in Time Series Classification

Junhao Yu, Fuyuan Xiao, *Senior Member, IEEE*, Yi Zhang, Zehong Cao, *Senior Member, IEEE*, and Chin-Teng Lin, *Fellow, IEEE*

***Abstract*—Time series classification (TSC) is a critical area with broad applications. In the field of evidence theory, quantum evidence theory (QET) offers a promising framework for one-dimensional TSC tasks, leveraging the capabilities of quantum basic probability amplitude (QBPA) to capture two-dimensional uncertainty. However, as the first step for the application of QET to TSC, how to construct QBPA still remains an open issue. In this paper, a novel approach to generate QBPA is devised. Specifically, we first apply the discrete Fourier transform (DFT) to the original data, extracting two-dimensional features embedded in the magnitude and phase from the frequency domain based on the front-few multi-frequency components, achieved by setting a threshold frequency index (TFI) to limit the frequencies considered. Next, we introduce the complex dual gaussian fuzzy number (CDGFN) as a carrier for QBPA, effectively representing two-dimensional uncertainty in the data. A CDGFN-based multisource information fusion (CDGFN-MSIF) algorithm for decision-making is proposed to combine information from different frequency components. Finally, the decision-making algorithm is validated on multiple time series datasets. Experimental results highlight the superior performance of the proposed approach over other state-of-the-art models, demonstrating its effectiveness and enhanced classification accuracy.**

***Index Terms*—Quantum evidence theory, time series classification, quantum basic probability amplitude, discrete Fourier transform, Gaussian fuzzy number, complex fuzzy number.**

I. INTRODUCTION

CLASSIFYING targets from data with temporal ordering, known as time series classification (TSC), is crucial in data mining and machine learning [1], [2]. Recent studies have also explored temporal association rule mining [3], [4] and efficient semi-supervised clustering [5] on multivariate time series, further highlighting the importance of temporal data analysis. This is especially relevant given the growing availability of temporal data in diverse applications [6] and the development of scalable infrastructure in diverse applications [7]. TSC enables the identification and categorization of patterns within sequential data, which is essential for applications like human activity recognition [8], anomaly detection [9], [10], and medical diagnosis [11]. However, TSC faces significant challenges due to inherent uncertainties in time series data [12]. These uncertainties not only affect classification reliability but also demand methods capable of reasoning under uncertainty [13], [14]. Therefore, TSC can be reframed as a problem of reasoning uncertainty in sequential data.

Recently, the challenge of effectively managing uncertainty has attracted much attention [15], [16], [17]. Uncertainty, inherent in various real-world scenarios, necessitates robust methodologies for its modeling and quantification [18], [19]. To address this, a plethora of approaches have been developed, each offering unique perspectives and tools for handling uncertain information, including fuzzy sets [20], rough sets [21], D number [22], evolutionary games [23], [24], Dempster-Shafer (D-S) evidence theory [25], [26], and others [27], [28], [29], [30]. Among those, D-S evidence theory has emerged as a particularly effective framework for managing uncertainty [31]. D-S evidence theory distinguishes itself by its ability to combine evidence from different sources and to represent ignorance explicitly, which is often not possible in traditional probabilistic approaches.

The versatility of D-S evidence theory has led to a wide range of research endeavors aimed at exploring its theoretical foundations and practical applications. Studies have delved into various aspects of the theory, including evidence reasoning [32], [33], belief rule base [34], complex evidence theory [35], random permutation sets [36], [37], [38], [39], [40], divergence [41], [42], [43], entropy [44], [45], distance [46], and fractal analysis [47], [48]. Beyond theoretical advancements, D-S evidence theory has found practical applications across diverse fields, such as expert system [49], [50], decision making [51], [52], [53], rescuer assignments [54], risk and reliability assessment [55], [56], classification and clustering [57], [58], and others [59].

Received 15 June 2024; revised 19 December 2025; accepted 26 December 2025. Date of publication 12 January 2026; date of current version 13 February 2026. This work was supported in part by the National Natural Science Foundation of China under Grant 62473067, in part by Xiaomi Young Talents Program, Chongqing Talents: Exceptional Young Talents Project under Grant cstc2022ycjh-bgzxm0070, in part by Chongqing Overseas Scholars Innovation Program under Grant cx2022024, and in part by Australian Research Council (ARC) Projects under Grant DE220100265, Grant DP250103612, and Grant LP240200636. Recommended for acceptance by Y. Gao. *(Corresponding author: Fuyuan Xiao.)*

Junhao Yu, Fuyuan Xiao, and Yi Zhang are with the School of Big Data and Software Engineering, Chongqing University, Chongqing 401331, China (e-mail: xiaofuyuan@cqu.edu.cn; doctorxiaofy@hotmail.com).

Zehong Cao is with the School of CSIT, Adelaide University, Adelaide, SA 5095, Australia (e-mail: zhcaonctu@gmail.com).

Chin-Teng Lin is with the Australia AI Institute, School of Computer Science, Faculty of Engineering and IT, University of Technology Sydney, Sydney, NSW 2007, Australia (e-mail: Chin-Teng.Lin@uts.edu.au).

Digital Object Identifier 10.1109/TKDE.2026.3652983

Classical D-S evidence theory faces limitations in handling two-dimensional features, which restricts its effectiveness in complex tasks like time series classification (TSC). TSC often requires extracting features embedded in the data to capture temporal patterns accurately. For example, Schäfer et al. [60] used the discrete Fourier transform (DFT) to extract frequency-domain features from time series data, allowing patterns to be represented in complex number space. Building on this approach, a quantum evidence theory (QET), proposed by Xiao [61], [62], addresses D-S theory's limitations by handling uncertainty within a complex number field. QET uses the quantum basic probability amplitude (QBPA), a complex number in Euler form with both magnitude and phase components, to represent two-dimensional information [63]. Furthermore, inspired by quantum constructive interference, QET incorporates a quantum evidential combination rule (QECR), enabling it to fuse information from multiple frequency components effectively. Applying QET to time series classification through DFT offers a novel approach to extract essential features and address uncertainty, making it a promising framework for TSC tasks.

However, as a prerequisite and core part of QET, the generation of QBPA still remains an open issue. In the previous works, most efforts have concentrated on modeling one-dimensional, real-valued BPA, exemplified by several seminal works. For example, a method to construct BPA based on triangular fuzzy number (TFN) was introduced in [64]; a method to construct BPA based on Gaussian fuzzy number (GFN) was introduced in [65]. These approaches have limitations in feature extraction, as they can only capture one-dimensional uncertainty. Furthermore, this point-to-point feature extraction is not suitable for handling one-dimensional time series data with misaligned time points.

To address these limitations, we propose a novel pipeline for one-dimensional TSC using multi-source information fusion within the QET framework. Specifically, we firstly propose a new method that leverages discrete Fourier transform (DFT) in the frequency domain to capture two-dimensional features (magnitude and phase) from only the lower, more informative multi-frequency components, achieved by setting a threshold frequency index (TFI). This approach enhances feature quality by focusing on useful information and discarding high-frequency noise. Based on this, we introduce the complex dual Gaussian fuzzy number (CDGFN) to generate QBPA, which effectively represents uncertainty in two dimensions. We then design a CDGFN-based multi-source information fusion (CDGFN-MSIF) algorithm to improve decision-making by combining information from different frequency components. Finally, we perform ablative studies to evaluate the contribution of each component within the proposed method, and compare its performance against several other classification techniques on well-established TSC datasets. The main contributions of this paper can be outlined as follows:

1) A two-dimensional frequency-domain feature extraction method is proposed, focusing on the magnitude and phase of complex numbers, specifically within the lower frequency range.
2) After that, a new approach to generate QBPA using CDGFN is proposed. The CDGFN can fully express two-dimensional uncertainty of magnitude and phase, which improves the precision of uncertainty modeling of QBPA under uncertain situations.
3) Then, a CDGFN-MSIF algorithm for enhancing decision-making ability is designed, which shows promising potential to reason uncertainty by combining information from multiple frequency components.

The rest of this paper is structured as follows. Section II reviews related work on relevant classification methods. Section III introduces relevant background knowledge. In Section IV, the details of the method to generate QBPA and the CDGFN-MSIF decision-making algorithm are elaborated. Section V applies the proposed method to established datasets to assess its performance. Section VI concludes this paper.

II. RELATED WORK

A. Deep-Learning-Based TSC Methods

Various deep learning approaches have been applied to time series classification (TSC). Multi-Layer Perceptron (MLP) [66] uses simple multiple layers to learn temporal patterns. Subsequent works use more powerful CNN architecture to extract features [67], [68]. Multi-scale Convolutional Neural Network (MCNN) [69] captures features at multiple scales by applying convolutional filters of various sizes. Time Le-Net (t-LeNet) [70] enhances classification by incorporating local pooling layers and data augmentation techniques. Multi-Channel Deep Convolutional Neural Network (MCDCNN) [71] is designed to handle multivariate time series data by processing each channel independently, allowing it to capture distinct features across multiple dimensions. Besides CNN-based models, functional echo state networks [72] and instance-attention graph neural networks (GNN) [73] have also been investigated for effective time series modeling. Despite their strengths, these deep learning models generally require large amounts of labeled data, and their performance often declines when faced with limited data sizes. Conversely, the proposed method can maintain high performance even with small datasets.

B. Evidence-Theory-Based Classification Methods

TSC is a type of classification tasks and the proposed method is within the evidence theory framework, making evidence-theory-based classification methods a viable comparison baseline. Recent advancements in evidential reasoning, such as the basic probability assignment (BPA) generation methods based on TFN [64] and GFN [65], have demonstrated significant progress in handling uncertainty. However, these methods have limited capability for processing complex, two-dimensional features and misaligned time series data due to their reliance on point-to-point extraction. Furthermore, the BPA values generated by TFN and GFN are real-valued, which restricts their applicability in frameworks like QET. In contrast, the proposed method, also rooted in evidence theory, extracts aligned two-dimensional features in the frequency domain and generates

TABLE I
SUMMARY OF IMPORTANT MATHEMATICAL NOTATIONS

Indices	
K	length of time series sequence
$\widetilde{\zeta}$	upper bound of extracted frequency range
P	number of classes
$N_{\mathcal{W}_p}$	number of samples for class $\mathcal{W}_p$
δ	predicted class index ($\delta \in \{1, \ldots, P\}$)
Parameters	
Ω	quantum frame of discernment (QFOD)
2^{Ω}	power set of QFOD Ω
$\mathcal{W}_p$	class representation for the p_{th} class in Ω
$\mathbb{Q}_{\mathbb{M}_{\widetilde{k}}}$	QBPA generated at the $\widetilde{k}_{th}$ frequency
$\mathbf{M}$	QBPD generated from the combination of QBPAs
$BetQP(\mathcal{W}_p)$	quantum Pignistic probability of class $\mathcal{W}_p$
$\widetilde{\mathcal{X}}_{\mathcal{W}_p n}^{\widetilde{K}}$	frequency sequence of the n_{th} sample for class $\mathcal{W}_p$ with length $\widetilde{K}$
$\widetilde{x}_{\mathcal{W}_p n}^{\widetilde{k}}$	the k_{th} frequency data point of the n_{th} sample for class $\mathcal{W}_p$
$\widetilde{\hat{x}}^{k}$	the k_{th} frequency data point of a test sample
$\mathcal{O}$	feature proxy ($\mathcal{O} \in \{\alpha, \theta\}$)
$\mathcal{O}_{\mathcal{W}_p n}^{\widetilde{k}}$	value of feature proxy $\mathcal{O}$ of the $\widetilde{k}_{th}$ frequency data point of the n_{th} sample for class $\mathcal{W}_p$
$\mathcal{S}$	statistic proxy ($\mathcal{S} \in \{\mu, \sigma\}$)
$\mathcal{S}_{\mathcal{W}_p}^{\widetilde{k}\mathcal{O}}$	statistic value with respect to statistic proxy $\mathcal{S}$ of feature proxy $\mathcal{O}$ at the $\widetilde{k}_{th}$ frequency of class $\mathcal{W}_p$
$f_{\mathcal{W}_p}^{\widetilde{k}\mathcal{O}}$	GFN membership function of feature proxy $\mathcal{O}$ at the $\widetilde{k}_{th}$ frequency for class $\mathcal{W}_p$
$f_{\mathcal{W}_p}^{\widetilde{k}}$	CDGFN membership function at the $\widetilde{k}_{th}$ frequency for class $\mathcal{W}_p$

complex-valued BPA, offering a more effective solution for TSC tasks.

III. PRELIMINARIES

The relevant background knowledge is detailed in this section. To enhance the readability of the proposed method, important mathematical notations used in this paper are summarized in Table I.

A. Quantum Evidence Theory

The quantum evidence theory (QET) integrates quantum concepts into D-S evidence theory [61], [62], [63].

Definition 1: Quantum frame of discernment

Let Ω be a set of mutually exclusive and collective nonempty sets. $\mathcal{W}_p$ represents a single event in a Hilbert space $\mathcal{H}$. The quantum frame of discernment (QFOD) is defined by [61], [62], [63]:

$$\Omega = \{\mathcal{W}_1, \mathcal{W}_2, \ldots, \mathcal{W}_p, \ldots, \mathcal{W}_P\}, \tag{1}$$

its power set 2^{Ω} can be defined as

$$2^{\Omega} = \{\emptyset, \{\mathcal{W}_1\}, \{\mathcal{W}_2\}, \ldots, \{\mathcal{W}_1, \mathcal{W}_2\}, \ldots, \Omega\}, \tag{2}$$

where $\emptyset$ denotes the unknown event set.

Definition 2: Quantum mass function

In a quantum frame of discernment Ω, a quantum mass function (QMF) $\mathbb{Q}_{\mathbb{M}}$, also called quantum basic probability amplitude (QBPA), is represented as a complex number following a mapping rule [61], [62], [63]:

$$\mathbb{Q}_{\mathbb{M}} : 2^{\Omega} \rightarrow \mathbb{C}, \tag{3}$$

which satisfies

$$\begin{aligned} &\mathbb{Q}_{\mathbb{M}}(\emptyset) = 0, \\ &\mathbb{Q}_{\mathbb{M}}(\mathcal{W}_p) = \varphi(\mathcal{W}_p) e^{i\theta(\mathcal{W}_p)}, \quad \mathcal{W}_p \subseteq \Omega, \\ &\sum_{\mathcal{W}_p \subseteq \Omega} |\mathbb{Q}_{\mathbb{M}}(\mathcal{W}_p)|^2 = 1, \end{aligned} \tag{4}$$

in which $i = \sqrt{-1}$; $\varphi(\mathcal{W}_p) \in [0, 1]$ denotes the magnitude of $\mathbb{Q}_{\mathbb{M}}(\mathcal{W}_p)$; $\theta(\mathcal{W}_p)$ denotes the phase of $\mathbb{Q}_{\mathbb{M}}(\mathcal{W}_p)$; and $|\mathbb{Q}_{\mathbb{M}}(\mathcal{W}_p)|^2 = \varphi(\mathcal{W}_p)^2 \in [0, 1]$ represents the support degree to proposition $\mathcal{W}_p$.

In (4), $\mathbb{Q}_{\mathbb{M}}(\mathcal{W}_p)$ is also expressed as

$$\mathbb{Q}_{\mathbb{M}}(\mathcal{W}_p) = x + yi, \tag{5}$$

its square of magnitude can be represented as

$$|\mathbb{Q}_{\mathbb{M}}(\mathcal{W}_p)|^2 = \varphi(\mathcal{W}_p)^2 = \mathbb{Q}_{\mathbb{M}}(\mathcal{W}_p)\widehat{\mathbb{Q}}_{\mathbb{M}}(\mathcal{W}_p) = x^2 + y^2, \tag{6}$$

in which $\widehat{\mathbb{Q}}_{\mathbb{M}}(\mathcal{W}_p) = x - yi$ is the conjugate of $\mathbb{Q}_{\mathbb{M}}(\mathcal{W}_p)$. If $|\mathbb{Q}_{\mathbb{M}}(\mathcal{W}_p)|^2 > 0$, $\mathcal{W}_p$ is called a quantum focal element.

Definition 3: Quantum basic probability distribution

The quantum basic probability distribution (QBPD) of $\mathbb{Q}_{\mathbb{M}}$, can be defined as [61], [62], [63]:

$$\mathbf{M} : \quad 2^{\Omega} \rightarrow [0, 1], \tag{7}$$

which satisfies

$$\begin{aligned} &\mathbf{M}(\emptyset) = 0, \\ &\mathbf{M}(\mathcal{W}_p) = |\mathbb{Q}_{\mathbb{M}}(\mathcal{W}_p)|^2, \quad \mathcal{W}_p \subseteq \Omega; \\ &\sum_{\mathcal{W}_p \subseteq \Omega} \mathbf{M}(\mathcal{W}_p) = 1, \end{aligned} \tag{8}$$

where $\mathbf{M}(\mathcal{W}_p)$ represents the support degree assigned to proposition $\mathcal{W}_p$.

Definition 4: Quantum evidential combination rule

Let $\{\mathbb{Q}_{\mathbb{M}_1}, \ldots, \mathbb{Q}_{\mathbb{M}_k}, \ldots, \mathbb{Q}_{\mathbb{M}_K}\}$ be a set of QBPAs with proposition $\mathcal{W}_p$ within the QFOD Ω. The quantum evidential combination rule (QECR) is defined by [61], [62]

$$\begin{aligned} &\mathbb{Q}_{\mathbb{M}_1} \oplus \ldots \oplus \mathbb{Q}_{\mathbb{M}_k} \oplus \ldots \oplus \mathbb{Q}_{\mathbb{M}_K}(\mathcal{W}_p) = \frac{\mathbb{H}}{\mathbb{V}}, \\ &\mathbb{Q}_{\mathbb{M}_1} \oplus \ldots \oplus \mathbb{Q}_{\mathbb{M}_k} \oplus \ldots \oplus \mathbb{Q}_{\mathbb{M}_K}(\emptyset) = 0, \end{aligned} \tag{9}$$

which satisfies

$$\begin{aligned} &\mathbb{H} = \left| \sum_{\cap \mathcal{W}_{\mathcal{C}} = \mathcal{W}_p} \prod_{1 \leq k \leq K} \mathbb{Q}_{\mathbb{M}_k}(\mathcal{W}_{\mathcal{C}}) \right|^2, \\ &\mathbb{V} = \sum_{\mathcal{W}_{\mathcal{C}} \subseteq \Omega} \left| \sum_{\cap \mathcal{W}_{\mathcal{C}} = \mathcal{W}_p} \prod_{1 \leq k \leq K} \mathbb{Q}_{\mathbb{M}_k}(\mathcal{W}_{\mathcal{C}}) \right|^2, \end{aligned} \tag{10}$$

With Definition 3, the combined result also represents the QBPD $\mathbf{M}$ of proposition $\mathcal{W}_p$. Thus, the (9) can also be denoted as [61], [62]:

$$\mathbf{M}(\mathcal{W}_p) = \mathbb{Q}_{\mathbb{M}_1} \oplus \ldots \oplus \mathbb{Q}_{\mathbb{M}_k} \oplus \ldots \oplus \mathbb{Q}_{\mathbb{M}_K}(\mathcal{W}_p). \tag{11}$$

Definition 5: Quantum Pignistic transformation

Let $\mathbb{Q}_{\mathbb{M}}$ be a QBPA on QFOD Ω and $\mathcal{W}_p$ be a quantum proposition with $\mathcal{W}_p \in \Omega$. The quantum Pignistic transformation (QPT), denoted as $BetQP$, is defined as [61], [62]:

$$BetQP(\mathcal{W}_p) = \sum_{\substack{\mathcal{W}_p \cap \mathcal{W}_\mathcal{C} \neq \emptyset \\ \mathcal{W}_\mathcal{C} \subseteq \Omega}} |\mathbb{Q}_{\mathbb{M}}(\mathcal{W}_p)|^2 \cdot \frac{|\mathcal{W}_p \cap \mathcal{W}_\mathcal{C}|}{|\mathcal{W}_\mathcal{C}|}, \tag{12}$$

where $|\cdot|$ is the cardinality function. Since $\mathbf{M} = |\mathbb{Q}_{\mathbb{M}}|^2$, (12) can be simplified to

$$BetQP(\mathcal{W}_p) = \sum_{\substack{\mathcal{W}_p \cap \mathcal{W}_\mathcal{C} \neq \emptyset \\ \mathcal{W}_\mathcal{C} \subseteq \Omega}} \mathbf{M}(\mathcal{W}_p) \cdot \frac{|\mathcal{W}_p \cap \mathcal{W}_\mathcal{C}|}{|\mathcal{W}_\mathcal{C}|}. \tag{13}$$

B. Discrete Fourier Transform

Definition 6: Discrete Fourier transform

Let a K-point signal $\mathcal{X}^K = \{x^1, \ldots, x^k, \ldots, x^K\}$ of $K \in \mathbb{N}$ data points $x^k \in \mathbb{R}$ in time domain. Then, the DFT [74] of the signal $\mathcal{X}^K$ is defined by a sequence $\widetilde{\mathcal{X}}^{\widetilde{K}} = \{\widetilde{x}^{\widetilde{k}}\}_{\widetilde{k}=1}^{\widetilde{K}}$ of $\widetilde{K} \in \mathbb{N}$ complex data points $\widetilde{x}^{\widetilde{k}} \in \mathbb{C}$, denoted as

$$\widetilde{x}^{\widetilde{k}} = \sum_{k=1}^{K} x^k e^{-i\frac{2\pi}{K}k\widetilde{k}}, \quad i = \sqrt{-1}. \tag{14}$$

For clarity, in this paper, we use $\widetilde{\cdot}$ to distinguish frequency domain representations. Notably, the hat notation on $\widetilde{K}$ and $\widetilde{k}$ is only used to denote indices in the frequency domain, while their values remain in $\mathbb{R}$.

C. Fuzzy Number

Fuzzy number is a powerful tool for representing uncertainty. A brief introduction to Gaussian fuzzy number (GFN) and complex fuzzy number (CFN) [75] is given.

1) Gaussian Fuzzy Number:

Definition 7: GFN membership function

Let $\mathcal{W}_p$ be an event defined on a Hilbert space $\mathcal{H}$. For a sample x under the space $\mathcal{H}$, the membership degree of x in $\mathcal{W}_p$ is defined by

$$M_{\mathcal{W}_p}(x) = e^{-\frac{(x-\mu)^2}{2\sigma^2}}, \tag{15}$$

where $M_{\mathcal{W}_p}(x) \in [0, 1]$; μ denotes the mean and σ denotes the standard deviation. A higher $M_{\mathcal{W}_p}(x)$ indicates a greater likelihood of x belonging to $\mathcal{W}_p$.

2) Complex Fuzzy Number:

Definition 8: CFN membership function

Let $\mathcal{W}_p$ be an event defined on a Hilbert space $\mathcal{H}$. For a sample x to be discerned within $\mathcal{H}$, the complex-valued membership degree of x in $\mathcal{W}_p$ is defined by

$$C_{\mathcal{W}_p}(x) = \alpha_{\mathcal{W}_p}(x) e^{i\theta_{\mathcal{W}_p}(x)}, \tag{16}$$

where $\alpha_{\mathcal{W}_p}(x)$ denotes the magnitude of $C_{\mathcal{W}_p}(x)$, while $\theta_{\mathcal{W}_p}(x)$ denotes the phase of $C_{\mathcal{W}_p}(x)$. A higher $|C_{\mathcal{W}_p}(x)|$ implies that x is more likely to belong to $\mathcal{W}_p$.

IV. THE PROPOSED QBPA GENERATION METHOD AND DECISION-MAKING ALGORITHM

In this section, a new QBPA generation method and CDGFN-MSIF decision-making algorithm is proposed. The proposed method consists of four main steps: i) two-dimensional features are extracted in the frequency domain from the training dataset; ii) Gaussian fuzzy number (GFN) membership function models are established using the mean and standard deviation of the extracted features; iii) QBPA is generated for the test samples using the established GFN function model; and iv) the final classification decision is made using the CDGFN-MSIF algorithm to fuse QBPA. The whole pipeline is displayed in Fig. 1. In the following sections, each key component of the method, including the concept of CDGFN, will be detailed.

A. Feature Extraction

One key characteristic of time series data is the misalignment of time points. Direct extraction of features from the time domain can significantly reduce the credibility of features at identical time points, which negatively impacts the final fusion results. To enhance feature credibility, a detailed method for extracting features in the frequency domain is presented.

1) Features in Frequency Domain: In frequency domain analysis, every data point corresponds to information at a particular frequency. These frequencies are aligned and collectively contribute to depicting the overall characteristics of time series data. Once transformed into the frequency domain via DFT, each data point is represented as a complex number in Eulerian form. This representation includes a magnitude term, indicating the intensity of the data at a specific frequency, and a phase term, which provides information about the temporal periodicity of the data within that frequency component. Consequently, the magnitude and phase term serve as a distinct two-dimensional feature set for characterizing time series data. Therefore, the selected features in the frequency domain will be defined by the magnitude and phase values.

2) Using Front-Few Frequencies: Suppose $\mathcal{X}^K = \{x^1, \ldots, x^k, \ldots, x^K\}$ is a time series sequence of length K. The corresponding data after applying the DFT to $\mathcal{X}^K$ is denoted by $\widetilde{\mathcal{X}}^{\widetilde{K}} = \{\widetilde{x}^{\widetilde{1}}, \ldots, \widetilde{x}^{\widetilde{k}}, \ldots, \widetilde{x}^{\widetilde{K}}\}$. Due to the properties of the DFT algorithm, the data in the first $\frac{\widetilde{K}}{2}$ and the second $\frac{\widetilde{K}}{2}$ segments are nearly conjugate to each other. when $\widetilde{K}$ is even, $\widetilde{\mathcal{X}}^{\widetilde{K}}$ follows this rule except for the $\widetilde{1}_{st}$ and $\left(\widetilde{\frac{K+2}{2}}\right)_{th}$ data. For odd $\widetilde{K}$, $\widetilde{X}^{\widetilde{K}}$ still adheres to this pattern except for the $\widetilde{1}_{st}$ element. This property results in identical magnitudes but opposite phase angles between these two segments. A numerical example is provided to illustrate this point.

Example 1: Assume two data sequences $\mathcal{X}^6$ and $\mathcal{X}^7$ with lengths of 6 (even) and 7 (odd), respectively:

$$\mathcal{X}^6 = \{1.3, 2.4, 3.0, -9, 4, 1.3\},$$

$$\mathcal{X}^7 = \{10.0, 3.0, 2.1, 4.5, 8.9, 0.23, -3.2\}.$$

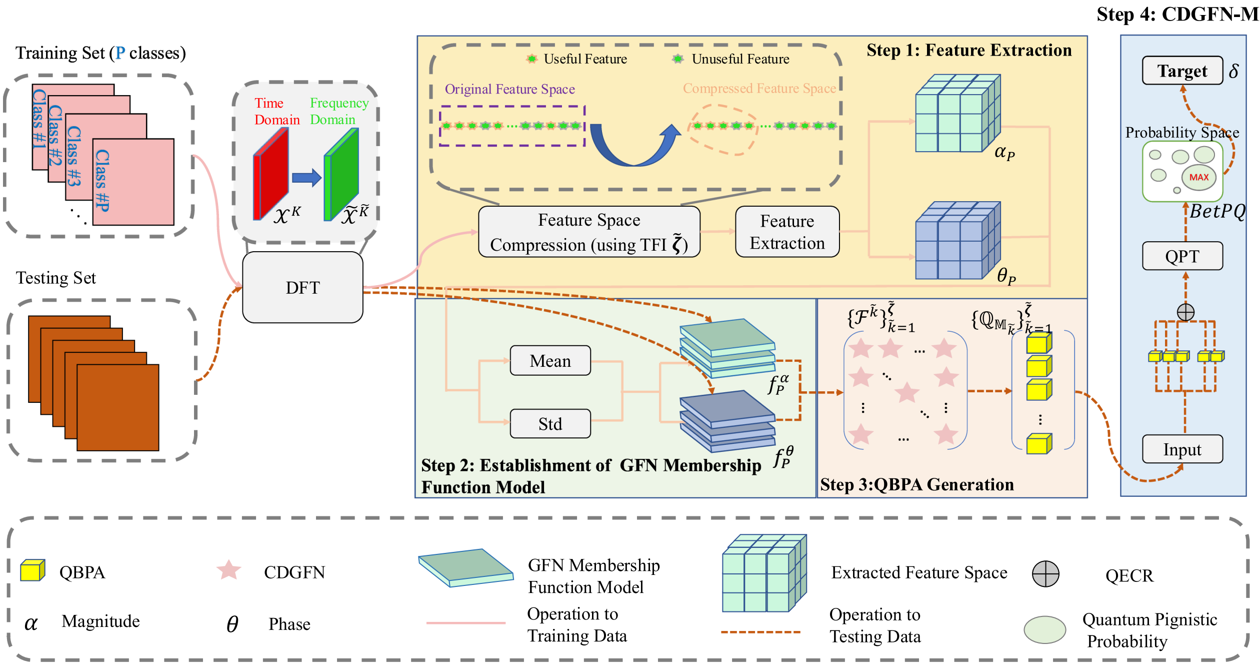

Fig. 1. Overview of the proposed method.

Then, with (14), $\mathcal{X}^6$ and $\mathcal{X}^7$ are transformed to $\widetilde{\mathcal{X}}^6$ and $\widetilde{\mathcal{X}}^7$, respectively:

$$\begin{aligned}\widetilde{\mathcal{X}}^6 = \big\{&3.00e^{0.00i}, 8.65e^{-0.01i}, 13.18e^{-3.00i},\\ &13.60e^{0.00i}, 13.18e^{3.00i}, 8.65^{0.01i}\big\},\\ \widetilde{\mathcal{X}}^7 = \big\{&25.53e^{0.00i}, 5.48e^{-2.09i}, 18.46e^{-0.49i},\\ &9.18e^{0.34i}, 9.18e^{-0.34i}, 18.46e^{0.49i},\\ &5.48e^{2.09i}\big\}.\end{aligned}$$

Observing the first result $\widetilde{\mathcal{X}}^6$, we find that the coefficients are conjugate to each other, except for the $\widetilde{1}_{st}$ and $\widetilde{4}_{th}$ elements. In the second result $\widetilde{\mathcal{X}}^7$, the rule is still obeyed. Hence, the features extracted from the first $\frac{\widetilde{K}}{2}$ segments are mirrored in the second $\frac{\widetilde{K}}{2}$ segments. Therefore, only the data from the first $\frac{\widetilde{K}}{2}$ segments is used to extract the two-dimensional features.

According to [76], the front-few frequencies contain essential information for characterizing time series data, while high frequencies contribute mostly to noise. Inspired by this, a threshold frequency index (TFI) $\widetilde{\zeta}$ $\left(\widetilde{\zeta} \ll \frac{\widetilde{K}}{2}\right)$ obtained from enumeration on the whole frequency space is set to specify the maximum frequency for feature extraction. Consequently, only features with a frequency index less than or equal to $\widetilde{\zeta}$ are extracted for analysis. Experimental results indicate that highest accuracy is often achieved with very small TFI $\widetilde{\zeta}$. More details on selecting the optimal TFI $\widetilde{\zeta}$ for a specific dataset are presented in Section V. The detailed feature extraction process is as follows.

Assume there are $P \in \mathbb{N}$ classes in the original dataset $\mathcal{R}^K$ with length $K \in \mathbb{N}$, described by the QFOD: $\Omega = \{\mathcal{W}_1, \ldots, \mathcal{W}_p, \ldots, \mathcal{W}_P\}$. The original data $\mathcal{R}^K$ is pre-split into a training set $\mathcal{X}^K$ and a testing set $\hat{\mathcal{X}}^K$, where the hat notation $\hat{\cdot}$ distinguishes the testing set from the training set. Considering the P classes, the training set $\mathcal{X}^K$ is further divided as $\mathcal{X}^K = \{\mathcal{X}^K_{\mathcal{W}_p}\}_{p=1}^P$. For a specific subdataset $\mathcal{X}^K_{\mathcal{W}_p}$, the number of samples is represented by $N_{\mathcal{W}_p} \in \mathbb{N}$. Then, each class dataset $\mathcal{X}^K_{\mathcal{W}_p}$ can be further divided as

$$\mathcal{X}^K_{\mathcal{W}_p} = \{\mathcal{X}^K_{\mathcal{W}_p 1}, \ldots, \mathcal{X}^K_{\mathcal{W}_p n}, \ldots, \mathcal{X}^K_{\mathcal{W}_p N_{\mathcal{W}_p}}\}, \tag{17}$$

where a single time series sequence is denoted as $\mathcal{X}^K_{\mathcal{W}_p n} = \{x^k_{\mathcal{W}_p n}\}_{k=1}^K$ consisting of K data points $x^k_{\mathcal{W}_p n} \in \mathbb{R}$ in time domain.

In frequency domain, the transformed training set is denoted as $\widetilde{\mathcal{X}}^{\widetilde{K}} = \{\widetilde{\mathcal{X}}^{\widetilde{K}}_{\mathcal{W}_p}\}_{p=1}^P$ of P transformed class dataset $\widetilde{\mathcal{X}}^{\widetilde{K}}_{\mathcal{W}_p} = \{\widetilde{\mathcal{X}}^{\widetilde{K}}_{\mathcal{W}_p n}\}_{n=1}^{N_{\mathcal{W}_p}}$ consisting of $N_{\mathcal{W}_p}$ of samples $\widetilde{\mathcal{X}}^{\widetilde{K}}_{\mathcal{W}_p n} = \{\widetilde{x}^{\widetilde{k}}_{\mathcal{W}_p n}\}_{\widetilde{k}=\widetilde{1}}^{\widetilde{K}}$ composed of $\widetilde{K}$ complex data points $\widetilde{x}^{\widetilde{k}}_{\mathcal{W}_p n} \in \mathbb{C}$ in the frequency domain. Each data point $\widetilde{x}^{\widetilde{k}}_{\mathcal{W}_p n} = \alpha^{\widetilde{k}}_{\mathcal{W}_p n} e^{i\theta^{\widetilde{k}}_{\mathcal{W}_p n}}$ consists of magnitude $\alpha^{\widetilde{k}}_{\mathcal{W}_p n} \in \mathbb{R}$, phase $\theta^{\widetilde{k}}_{\mathcal{W}_p n} \in \mathbb{R}$, and imaginary unit i. The frequency-domain feature space is defined as follows.

Definition 9: Frequency-domain feature space

Let $\mathcal{O}$ be the frequency-domain feature proxy of magnitude α and phase θ, denoted as

$$\mathcal{O} = \{\alpha, \theta\}. \tag{18}$$

For simplicity, we use $\mathcal{O}$ as a feature proxy for both α and θ in shared operations, since most operations apply to them in the same way. However, α and θ will be addressed separately where distinct treatment is required in later sections.

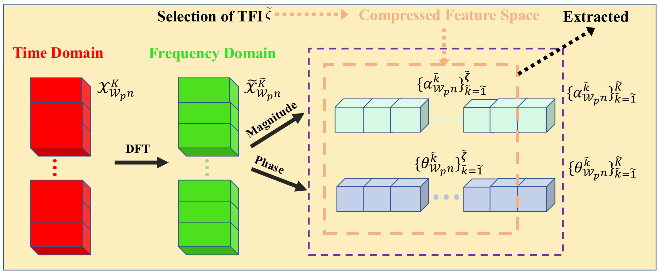

Fig. 2. A schematic representation of the process for extracting two-dimensional features for a single sample $\mathcal{X}^K_{\mathcal{W}_p n}$ (the n_{th} instance for class $\mathcal{W}_p$).

Then, the feature column vector $\mathcal{O}^{\widetilde{k}}_{\mathcal{W}_p} \in \mathbb{R}^{N_{\mathcal{W}_p}}$ of the proxy $\mathcal{O}$ at the $\widetilde{k}_{th}$ frequency for class $\mathcal{W}_p$ is denoted as

$$\mathcal{O}^{\widetilde{k}}_{\mathcal{W}_p} = \left\{\mathcal{O}^{\widetilde{k}}_{\mathcal{W}_p 1}, \mathcal{O}^{\widetilde{k}}_{\mathcal{W}_p 2}, \ldots, \mathcal{O}^{\widetilde{k}}_{\mathcal{W}_p n}, \ldots, \mathcal{O}^{\widetilde{k}}_{\mathcal{W}_p N_{\mathcal{W}_p}}\right\}, \tag{19}$$

where $\mathcal{O}^{\widetilde{k}}_{\mathcal{W}_p n}$ represents the value of feature proxy $\mathcal{O}$ at the $\widetilde{k}_{th}$ frequency of the n_{th} sample for class $\mathcal{W}_p$.

Consequently, the frequency-domain feature space of $\widetilde{\mathcal{X}}^{\widetilde{K}}_{\mathcal{W}_p}$ with respect to $\mathcal{O}$ across the front $\widetilde{\zeta}$ frequencies for class $\mathcal{W}_p$, i.e., $\mathcal{O}_{\mathcal{W}_p} \in \mathbb{R}^{N_{\mathcal{W}_p} \times \widetilde{\zeta}}$, can be denoted as

$$\mathcal{O}_{\mathcal{W}_p} = \left\{\mathcal{O}^{\widetilde{1}}_{\mathcal{W}_p}, \ldots, \mathcal{O}^{\widetilde{k}}_{\mathcal{W}_p}, \ldots, \mathcal{O}^{\widetilde{\zeta}}_{\mathcal{W}_p}\right\}. \tag{20}$$

Eventually, the frequency-domain feature space over the P classes $\mathcal{O}_P \in \mathbb{R}^{P \times N_{\mathcal{W}_p} \times \widetilde{\zeta}}$ can be denoted as

$$\mathcal{O}_P = \left\{\mathcal{O}_{\mathcal{W}_1}, \ldots, \mathcal{O}_{\mathcal{W}_p}, \ldots, \mathcal{O}_{\mathcal{W}_P}\right\}. \tag{21}$$

Below, a detailed procedure to extract two-dimensional features for a specific class $\mathcal{W}_p$ is presented.

Step 1: With (14), DFT is applied to the original training data $\mathcal{X}^K$ to obtain the transformed data $\widetilde{\mathcal{X}}^{\widetilde{K}}$ in the frequency domain.

Step 2: Then, the front $\widetilde{\zeta}$ values from $\widetilde{\mathcal{X}}^{\widetilde{K}}$, denoted as $\widetilde{\mathcal{X}}^{\widetilde{\zeta}}$ can be obtained, where TFI $\widetilde{\zeta}$ is selected by enumeration.

Step 3: With (20), the feature space for magnitude and phase across the front $\widetilde{\zeta}$ frequencies for class $\mathcal{W}_p$, represented by $\mathcal{O}_{\mathcal{W}_p} \in \mathbb{R}^{N_{\mathcal{W}_p} \times \widetilde{\zeta}}$ $(\mathcal{O} \in \{\alpha, \theta\})$ can be obtained

$$\mathcal{O}_{\mathcal{W}_p} = \left\{\mathcal{O}^{\widetilde{1}}_{\mathcal{W}_p}, \ldots, \mathcal{O}^{\widetilde{k}}_{\mathcal{W}_p}, \ldots, \mathcal{O}^{\widetilde{\zeta}}_{\mathcal{W}_p}\right\}, \tag{22}$$

where $\mathcal{O}^{\widetilde{k}}_{\mathcal{W}_p} = \left\{\mathcal{O}^{\widetilde{k}}_{\mathcal{W}_p n}\right\}_{n=1}^{N_{\mathcal{W}_p}}$ of $N_{\mathcal{W}_p}$ feature values $\mathcal{O}^{\widetilde{k}}_{\mathcal{W}_p n} \in \mathbb{R}$.

The feature extraction process is repeated for each class. Then, the complete frequency-domain feature space $\mathcal{O}_P \in \mathbb{R}^{P \times N_{\mathcal{W}_p} \times \widetilde{\zeta}}$ with respect to the transformed training set $\widetilde{\mathcal{X}}^{\widetilde{\zeta}}$ across the front $\widetilde{\zeta}$ frequencies for P classes can be obtained, denoted as

$$\mathcal{O}_P = \left\{\mathcal{O}_{\mathcal{W}_1}, \ldots, \mathcal{O}_{\mathcal{W}_p}, \ldots, \mathcal{O}_{\mathcal{W}_P}\right\}. \tag{23}$$

Since $\mathcal{O} \in \{\alpha, \theta\}$, the feature space of magnitude α_P and phase θ_P can be obtained. To better illustrate this process, Fig. 2 serves as a concrete example processing a single time series sequence. Starting with a specific n_{th} time series sample in class $\mathcal{W}_p$, denoted as $\mathcal{X}^K_{\mathcal{W}_p n}$. The process begins by transforming the time-domain signal into the frequency domain $\widetilde{\mathcal{X}}^{\widetilde{K}}_{\mathcal{W}_p n}$ using DFT. The resulting complex values are decomposed into magnitude (α) and phase (θ) components. Then, the two-dimensional features $\left\{\alpha^{\widetilde{k}}_{\mathcal{W}_p n}\right\}_{\widetilde{k}=\widetilde{1}}^{\widetilde{\zeta}}$ and $\left\{\theta^{\widetilde{k}}_{\mathcal{W}_p n}\right\}_{\widetilde{k}=\widetilde{1}}^{\widetilde{\zeta}}$ within the TFI $\widetilde{\zeta}$ are extracted.

B. Complex Dual Gaussian Fuzzy Number

In the frequency domain, two-dimensional features are extracted. However, GFN can only represent one-dimensional information, limiting its applicability to two-dimensional features. Additionally, the GFN operates in the real number field, which prevents it from leveraging the strengths of QET in the complex number field. To address this, an extended version called the complex dual Gaussian fuzzy number (CDGFN) is introduced, combining the strengths of CFN and GFN in handling uncertainty. Section IV-B1 details the motivations for combining GFN and CFN, while Section IV-B2 defines the CDGFN membership function.

1) Motivations: CFN is briefly introduced in Definition 8. Observing through its membership function, we can find that each CFN is composed of two parts: a magnitude term and a phase angle term. The magnitude term works like a traditional real-valued fuzzy number, indicating the degree of membership in a class. However, the phase term adds an extra layer of information, setting CFN apart from ordinary fuzzy numbers.

Using complex numbers as the medium for QBPA ensures that arithmetic operations, such as multiplication, addition, and division, are based on complex number principles. In QECR ((9)), different QBPAs interact during these operations, leading to constructive and destructive interference similar to quantum system behavior. This interference can make it difficult for QBPAs with low membership grades to remain consistent. This counterintuitive outcome is due to the phase component of complex numbers, represented by the imaginary unit i, associated with e (the base of the natural logarithm). This phase component captures uncertainty from an additional dimension, allowing CFN to represent more complex information.

The above discussion demonstrates that CFN can effectively represent two-dimensional uncertainty, making it a suitable medium for QBPA due to its complex fuzzy nature. Additionally, the magnitude of CFN is bounded within $[0, 1]$, aligning with QBPA's requirements. Meanwhile, a single GFN membership function is sufficient for expressing one-dimensional uncertainty. Therefore, by combining the strengths of GFN and CFN, the proposed CDGFN can comprehensively capture and express two-dimensional uncertainty, serving as an ideal carrier for QBPA.

2) CDGFN Membership Function: By integrating CFN and GFN, CDGFN is formed as a complex fuzzy number composed of two Gaussian fuzzy numbers. To define CDGFN, we outline key definitions in sequence: the statistic space, the GFN membership function for feature proxy $\mathcal{O}$, and the CDGFN membership function.

Definition 10: Statistic space

Let $\mathcal{S}$ be the statistic proxy of mean μ and standard deviation σ, denoted as

$$\mathcal{S} = \{\mu, \sigma\}. \tag{24}$$

Given a feature proxy $\mathcal{O}$ in the frequency domain, the statistical quantity of $\mathcal{S}$ at the $\widetilde{k}_{th}$ frequency for class $\mathcal{W}_p$ is denoted as $\mathcal{S}_{\mathcal{W}_p}^{\widetilde{k}\mathcal{O}} \in \mathbb{R}$. Then, the statistic space with respect to $\mathcal{S}$ of feature proxy $\mathcal{O}$ across the front $\widetilde{\zeta}$ frequencies for class $\mathcal{W}_p$ can be denoted as

$$\mathcal{S}_{\mathcal{W}_p}^{\mathcal{O}} = \left\{ \mathcal{S}_{\mathcal{W}_p}^{\widetilde{1}\mathcal{O}}, \ldots, \mathcal{S}_{\mathcal{W}_p}^{\widetilde{k}\mathcal{O}}, \ldots, \mathcal{S}_{\mathcal{W}_p}^{\widetilde{\zeta}\mathcal{O}} \right\}, \tag{25}$$

where $\mathcal{S}_{\mathcal{W}_p}^{\mathcal{O}} \in \mathbb{R}^{\widetilde{\zeta}}$.

Definition 11: GFN membership function for feature proxy $\mathcal{O}$

Let $\mathcal{W}_p$ be a class in QFOD Ω. Suppose $\widetilde{\hat{x}}$ is a transformed test sample with feature value $\mathcal{O}^{\widetilde{k}}$ of feature $\mathcal{O}$ at the $\widetilde{k}_{th}$ frequency. The GFN membership function $f_{\mathcal{W}_p}^{\widetilde{k}\mathcal{O}}(\widetilde{\hat{x}})$ is defined as

$$f_{\mathcal{W}_p}^{\widetilde{k}\mathcal{O}}\left(\widetilde{\hat{x}}\right) = e^{-\frac{\left(\mathcal{O}^{\widetilde{k}} - \mu_{\mathcal{W}_p}^{\widetilde{k}\mathcal{O}}\right)^2}{2\sigma_{\mathcal{W}_p}^{\widetilde{k}\mathcal{O}\,2}}}, \tag{26}$$

where $\mu_{\mathcal{W}_p}^{\widetilde{k}\mathcal{O}}$ and $\sigma_{\mathcal{W}_p}^{\widetilde{k}\mathcal{O}}$ are derived from substituting the statistical proxy $\mathcal{S}$ in (25) with mean μ and standard deviation σ, representing the mean and standard deviation of feature proxy $\mathcal{O}$ at the $\widetilde{k}_{th}$ frequency for class $\mathcal{W}_p$. The function $f_{\mathcal{W}_p}^{\widetilde{k}\mathcal{O}}(\widetilde{\hat{x}})$ is bounded within $[0, 1]$, with $\mathcal{O} \in \{\alpha, \theta\}$.

Definition 12: CDGFN membership function

Let $\mathcal{W}_p$ be a class in QFOD Ω. Suppose $\widetilde{\hat{x}}$ is a transformed test sample with feature values $\alpha^{\widetilde{k}}$ and $\theta^{\widetilde{k}}$ of magnitude and phase at the $\widetilde{k}_{th}$ frequency. The membership degree of $\widetilde{\hat{x}}$ at the $\widetilde{k}_{th}$ frequency for class $\mathcal{W}_p$ is defined by the CDGFN membership function, defined by

$$\begin{aligned} f_{\mathcal{W}_p}^{\widetilde{k}}(\widetilde{\hat{x}}) &= f_{\mathcal{W}_p}^{\widetilde{k}\alpha}(\widetilde{\hat{x}}) e^{i f_{\mathcal{W}_p}^{\widetilde{k}\theta}(\widetilde{\hat{x}})} \\ &= e^{-\frac{(\alpha^{\widetilde{k}} - \mu_{\mathcal{W}_p}^{\widetilde{k}\alpha})^2}{2\sigma_{\mathcal{W}_p}^{\widetilde{k}\alpha\,2}}} e^{ie^{-\frac{(\theta^{\widetilde{k}} - \mu_{\mathcal{W}_p}^{\widetilde{k}\theta})^2}{2\sigma_{\mathcal{W}_p}^{\widetilde{k}\theta\,2}}}}, \end{aligned} \tag{27}$$

where $\mu_{\mathcal{W}_p}^{\widetilde{k}\alpha}$, $\mu_{\mathcal{W}_p}^{\widetilde{k}\theta}$, $\sigma_{\mathcal{W}_p}^{\widetilde{k}\alpha}$ and $\sigma_{\mathcal{W}_p}^{\widetilde{k}\theta}$ are derived from substituting the statistical proxy $\mathcal{S}$ in (25) with $\{\mu, \sigma\}$, and the feature proxy $\mathcal{O}$ with $\{\alpha, \theta\}$, representing the respective mean and standard deviation values for magnitude and phase at the $\widetilde{k}_{th}$ frequency for class $\mathcal{W}_p$.

The modulus $|f_{\mathcal{W}_p}^{\widetilde{k}}(\widetilde{\hat{x}})|$ indicates the membership grade of $\widetilde{\hat{x}}$ in class $\mathcal{W}_p$. Since $f_{\mathcal{W}_p}^{\alpha\widetilde{k}}(\widetilde{\hat{x}})$ falls within $[0, 1]$, $|f_{\mathcal{W}_p}^{\widetilde{k}}(\widetilde{\hat{x}})|$ is also within in [0,1], following the properties of fuzzy numbers. A higher $|f_{\mathcal{W}_p}^{\widetilde{k}}(\widetilde{\hat{x}})|$ means a greater membership grade for $\widetilde{\hat{x}}$ in $\mathcal{W}_p$ at the $\widetilde{k}_{th}$ frequency.

C. Establishment of GFN Membership Function Model

CDGFN serves as the carrier for QBPA, which is de- rived from the GFN membership function values for both magnitude and phase components. To obtain QBPA, the GFN membership function must first be established using two- dimensional features.

In (23), two-dimensional feature space $\mathcal{O} = \{\mathcal{O}_{\mathcal{W}_p}\}_{p=1}^{P}$ of P subfeature spaces $\mathcal{O}_{\mathcal{W}_p} = \left\{\mathcal{O}_{\mathcal{W}_p}^{\widetilde{k}}\right\}_{\widetilde{k}=1}^{\widetilde{\zeta}}$ of $\widetilde{\zeta}$ feature column vectors $\mathcal{O}_{\mathcal{W}_p}^{\widetilde{k}} = \left\{\mathcal{O}_{\mathcal{W}_p n}^{\widetilde{k}}\right\}_{n=1}^{N_{\mathcal{W}_p}}$ have been collected. The GFN membership function model generation procedures across the front $\widetilde{\zeta}$ frequencies for feature proxy $\mathcal{O}$ are as follows.

1) With the extracted two-dimensional feature values $\left\{\mathcal{O}_{\mathcal{W}_p n}^{\widetilde{k}}\right\}_{n=1}^{N_{\mathcal{W}_p}}$, the mean and standard deviation of $\mathcal{O}$ at the $\widetilde{k}_{th}$ frequency for class $\mathcal{W}_p$ can be obtained according to following equations

$$\begin{aligned} \mu_{\mathcal{W}_p}^{\widetilde{k}\mathcal{O}} &= \frac{1}{N_{\mathcal{W}_p}} \sum_{n=1}^{N_{\mathcal{W}_p}} \mathcal{O}_{\mathcal{W}_p n}^{\widetilde{k}}, \\ \sigma_{\mathcal{W}_p}^{\widetilde{k}\mathcal{O}} &= \sqrt{\frac{1}{N_{\mathcal{W}_p} - 1} \sum\nolimits_{n=1}^{N_{\mathcal{W}_p}} \left(\mathcal{O}_{\mathcal{W}_p n}^{\widetilde{k}} - \mu_{\mathcal{W}_p}^{\widetilde{k}\mathcal{O}}\right)^2}. \end{aligned} \tag{28}$$

This process is repeated for the front $\widetilde{\zeta}$ frequencies to obtain the statistic space of feature proxy $\mathcal{O}$ for class $\mathcal{W}_p$, denoted as

$$\begin{aligned} \mu_{\mathcal{W}_p}^{\mathcal{O}} &= \left\{\mu_{\mathcal{W}_p}^{\widetilde{1}\mathcal{O}}, \ldots, \mu_{\mathcal{W}_p}^{\widetilde{k}\mathcal{O}}, \ldots, \mu_{\mathcal{W}_p}^{\widetilde{\zeta}\mathcal{O}}\right\}, \\ \sigma_{\mathcal{W}_p}^{\mathcal{O}} &= \left\{\sigma_{\mathcal{W}_p}^{\widetilde{1}\mathcal{O}}, \ldots, \sigma_{\mathcal{W}_p}^{\widetilde{k}\mathcal{O}}, \ldots, \sigma_{\mathcal{W}_p}^{\widetilde{\zeta}\mathcal{O}}\right\}. \end{aligned} \tag{29}$$

2) With (26), the GFN membership functions $f_{\mathcal{W}_p}^{\mathcal{O}}$of $\mathcal{O}$ for class $\mathcal{W}_p$ can be derived as follows

$$\left\{\mu_{\mathcal{W}_p}^{\mathcal{O}}, \sigma_{\mathcal{W}_p}^{\mathcal{O}}\right\} \longrightarrow f_{\mathcal{W}_p}^{\mathcal{O}}, \tag{30}$$

in which

$$f_{\mathcal{W}_p}^{\mathcal{O}} = \left\{f_{\mathcal{W}_p}^{\widetilde{1}\mathcal{O}}, \ldots, f_{\mathcal{W}_p}^{\widetilde{k}\mathcal{O}}, \ldots, f_{\mathcal{W}_p}^{\widetilde{\zeta}\mathcal{O}}\right\}, \tag{31}$$

where $f_{\mathcal{W}_p}^{\widetilde{k}\mathcal{O}}$ is a single GFN membership function of $\mathcal{O}$ at the $\widetilde{k}_{th}$ frequency for class $\mathcal{W}_p$, obtained as

$$\left\{\mu_{\mathcal{W}_p}^{\widetilde{k}\mathcal{O}}, \sigma_{\mathcal{W}_p}^{\widetilde{k}\mathcal{O}}\right\} \longrightarrow f_{\mathcal{W}_p}^{\widetilde{k}\mathcal{O}}. \tag{32}$$

This generation process is repeated across all P classes. Thus, the set of GFN membership function $f_P^{\mathcal{O}}$ is constructed as

$$f_P^{\mathcal{O}} = \left\{f_{\mathcal{W}_1}^{\mathcal{O}}, \ldots, f_{\mathcal{W}_p}^{\mathcal{O}}, \ldots, f_{\mathcal{W}_P}^{\mathcal{O}}\right\}. \tag{33}$$

Given that $\mathcal{O} \in \{\alpha, \theta\}$, the GFN membership function model of magnitude f_P^{α} and phase f_P^{θ} can be obtained. Similarly, Fig. 3 provides a step-by-step example of establishing the GFN membership function model for a specific class. For a given class $\mathcal{W}_p$, the extracted two-dimensional features $\alpha_{\mathcal{W}_p}$ and $\theta_{\mathcal{W}_p}$ are used to calculate the mean (μ) and standard deviation (σ). These calculated statistical values are used to construct the GFN membership function models for magnitude and phase, i.e., $f_{\mathcal{W}_p}^{\alpha}$ and $f_{\mathcal{W}_p}^{\theta}$.

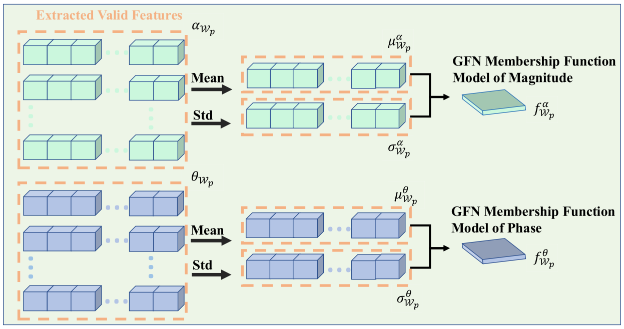

Fig. 3. A schematic representation of the process for constructing the GFN membership function model for a single class $\mathcal{W}_p$.

D. QBPA Generation

After obtaining the GFN membership functions described in Section IV-C, the next step is to generate QBPA for a specific test sample.

Assuming the GFN membership functions of $\mathcal{O}$ across the front $\widetilde{\zeta}$ frequencies for P classes have been constructed using (33), denoted as $f_P^{\mathcal{O}} = \{f_{\mathcal{W}_p}^{\mathcal{O}}\}_{p=1}^{P}$, where $f_{\mathcal{W}_p}^{\mathcal{O}} = \{f_{\mathcal{W}_p}^{\widetilde{k}\mathcal{O}}\}_{\widetilde{k}=\widetilde{1}}^{\widetilde{\zeta}}$. We extract the $\widetilde{k}_{th}$ function over $\{f_{\mathcal{W}_p}^{\mathcal{O}}\}_{p=1}^{P}$ to form the GFN membership function at the $\widetilde{k}_{th}$ frequency for P classes, denoted as $\{f_{\mathcal{W}_p}^{\widetilde{k}\mathcal{O}}\}_{p=1}^{P}$. Then, we substitute the $\mathcal{O}$ with magnitude α and phase θ after which the corresponding membership functions $\{f_{\mathcal{W}_p}^{\widetilde{k}\alpha}\}_{p=1}^{P}$ and $\{f_{\mathcal{W}_p}^{\widetilde{k}\theta}\}_{p=1}^{P}$ have been generated.

Suppose a testing sample from the pre-split testing set is represented as

$$\{\hat{x}^1, \ldots, \hat{x}^k, \ldots, \hat{x}^K\}. \tag{34}$$

The process for generating QBPA at a specific frequency $\widetilde{k}$ is detailed below.

1) Using (14), the Discrete Fourier Transform (DFT) is applied to the testing sample $\left\{\hat{x}^k\right\}_{k=1}^{K}$ to transform it from time domain to frequency domain, denoted as

$$\left\{\widetilde{\hat{x}}^{\widetilde{1}}, \ldots, \widetilde{\hat{x}}^{\widetilde{k}}, \ldots, \widetilde{\hat{x}}^{\widetilde{K}}\right\}. \tag{35}$$

2) Since TFI $\widetilde{\zeta}$ is selected from enumeration, the transformed testing data $\left\{\widetilde{\hat{x}}^{\widetilde{k}}\right\}_{\widetilde{k}=\widetilde{1}}^{\widetilde{K}}$ in the selected feature space can be denoted as:

$$\left\{\widetilde{\hat{x}}^{\widetilde{1}}, \ldots, \widetilde{\hat{x}}^{\widetilde{k}}, \ldots, \widetilde{\hat{x}}^{\widetilde{\zeta}}\right\}, \quad \widetilde{\hat{x}}^{\widetilde{k}} = \alpha^{\widetilde{k}} e^{i\theta^{\widetilde{k}}}. \tag{36}$$

3) With (26), input the magnitude and phase features of $\widetilde{\hat{x}}^{\widetilde{k}}$ into the established training GFN membership function $\{f_{\mathcal{W}_p}^{\widetilde{k}\alpha}\}_{p=1}^{P}$ and $\{f_{\mathcal{W}_p}^{\widetilde{k}\theta}\}_{p=1}^{P}$. The membership grades of magnitude and phase at the $\widetilde{k}_{th}$ frequency for P classes can be obtained

$$\mathcal{F}_P^{\widetilde{k}\alpha} = \left\{f_{\mathcal{W}_1}^{\widetilde{k}\alpha}(\widetilde{\hat{x}}^{\widetilde{k}}), \ldots, f_{\mathcal{W}_p}^{\widetilde{k}\alpha}(\widetilde{\hat{x}}^{\widetilde{k}}), \ldots, f_{\mathcal{W}_P}^{\widetilde{k}\alpha}(\widetilde{\hat{x}}^{\widetilde{k}})\right\},$$
$$\mathcal{F}_P^{\widetilde{k}\theta} = \left\{f_{\mathcal{W}_1}^{\widetilde{k}\theta}(\widetilde{\hat{x}}^{\widetilde{k}}), \ldots, f_{\mathcal{W}_p}^{\widetilde{k}\theta}(\widetilde{\hat{x}}^{\widetilde{k}}), \ldots, f_{\mathcal{W}_P}^{\widetilde{k}\theta}(\widetilde{\hat{x}}^{\widetilde{k}})\right\}. \tag{37}$$

4) With (27), the CDGFN membership at the $\widetilde{k}_{th}$ frequency for class $\mathcal{W}_p$ can be obtained

$$f_{\mathcal{W}_p}^{\widetilde{k}}\left(\widetilde{\hat{x}}\right) = f_{\mathcal{W}_p}^{\widetilde{k}\alpha}\left(\widetilde{\hat{x}}^{\widetilde{k}}\right) e^{i f_{\mathcal{W}_p}^{\widetilde{k}\theta}\left(\widetilde{\hat{x}}^{\widetilde{k}}\right)}. \tag{38}$$

Then, the CDGFN membership array at the $\widetilde{k}_{th}$ frequency for P classes is constructed as

$$\mathcal{F}_P^{\widetilde{k}} = \left\{f_{\mathcal{W}_1}^{\widetilde{k}}(\widetilde{\hat{x}}), \ldots, f_{\mathcal{W}_p}^{\widetilde{k}}(\widetilde{\hat{x}}), \ldots, f_{\mathcal{W}_P}^{\widetilde{k}}(\widetilde{\hat{x}})\right\}. \tag{39}$$

5) In QET, the square of the modulus of a QBPA represents the support degree as defined in Definition 2. Therefore, the elements in $\mathcal{F}_P^{\widetilde{k}}$ are sorted in descending order of their squared modulus. Suppose

$$|f_{\mathcal{W}_1}^{\widetilde{k}}(\widetilde{\hat{x}})|^2 > \ldots > |f_{\mathcal{W}_p}^{\widetilde{k}}(\widetilde{\hat{x}})|^2 > \ldots > |f_{\mathcal{W}_P}^{\widetilde{k}}(\widetilde{\hat{x}})|^2. \tag{40}$$

6) Then, with assignment law, the membership degrees at the $\widetilde{k}_{th}$ frequency for subsets in Ω can be obtained

$$\left\{\mathcal{M}^{\widetilde{k}}(\{\mathcal{W}_1\}), \mathcal{M}^{\widetilde{k}}(\{\mathcal{W}_1, \mathcal{W}_2\}), \ldots, \mathcal{M}^{\widetilde{k}}(\{\Omega\})\right\}, \tag{41}$$

which satisfies

$$\begin{aligned} &\mathcal{M}^{\widetilde{k}}(\{\mathcal{W}_1\}) = f_{\mathcal{W}_1}^{\widetilde{k}}(\widetilde{\hat{x}}),\\ &\mathcal{M}^{\widetilde{k}}(\{\mathcal{W}_1, \mathcal{W}_2\}) = f_{\mathcal{W}_2}^{\widetilde{k}}(\widetilde{\hat{x}}),\\ &\ldots\\ &\mathcal{M}^{\widetilde{k}}(\{\mathcal{W}_1, \mathcal{W}_2, \ldots, \mathcal{W}_P\}) = f_{\mathcal{W}_P}^{\widetilde{k}}(\widetilde{\hat{x}}), \end{aligned} \tag{42}$$

where $\mathcal{M}$ represents the membership degree of subsets in the QFOD Ω.

7) The QBPAs at the $\widetilde{k}_{th}$ frequency $\mathbb{Q}_{\mathbb{M}_{\widetilde{k}}}$ is generated after normalizing the membership degree, denoted as

$$\mathbb{Q}_{\mathbb{M}_{\widetilde{k}}} = \left\{\mathbb{Q}_{\mathbb{M}_{\widetilde{k}}}(\mathcal{A})\right\}_{\mathcal{A}\subseteq\Omega}, \tag{43}$$

in which

$$\mathbb{Q}_{\mathbb{M}_{\widetilde{k}}}(\mathcal{A}) = \frac{\mathcal{M}^{\widetilde{k}}(\mathcal{A})}{\sqrt{\sum_{\mathcal{A}\subseteq\Omega} |\mathcal{M}^{\widetilde{k}}(\mathcal{A})|^2}}. \tag{44}$$

For notational simplicity, we use the notation $\mathcal{A}$ to represent any possible grouping of classes, as seen in (42). For example, $\mathcal{A}$ could be $\{\mathcal{W}_1\}$, $\{\mathcal{W}_1, \mathcal{W}_2\}$, or any different subsets of classes in Ω.

It's learned that Jiang et al. [77] proposed a novel few-shot learning method named multi-scale metric learning, which significantly learns the multi-scale relations between samples. Deng et al. [78] proposed a new decision-level fusion approach to synthesize spectral, textural, structural features from multi-source remotely sensed data. Thus, QBPA generation process is repeated across the front $\widetilde{\zeta}$ frequencies to obtain $\widetilde{\zeta}$ sets of QBPA, denoted as $\mathcal{Q} = \left\{\mathbb{Q}_{\mathbb{M}_{\widetilde{k}}}\right\}_{\widetilde{k}=\widetilde{1}}^{\widetilde{\zeta}}$. The inclusion of multi-frequency information contributes to a more robust and reliable decision-making process. Next, the corresponding decision-making algorithm will be discussed.

Algorithm 1: QBPA Generation and CDGFN-MSIF Decision-Making Algorithm for Time Series Classification:

```
Input: QFOD: $\Omega = \{\mathcal{W}_1, \ldots, \mathcal{W}_p, \ldots, \mathcal{W}_P\}$
  TFI $\widetilde{\zeta}$: A frequency index obtained from enumeration.
  Training set: $\mathcal{X}^K$
Output: Classified target $\mathcal{W}_\delta$: the predicted class.
Transform training set to obtain $\widetilde{\mathcal{X}}^{\widetilde{K}}$ using Eq. (14).
Obtain the training set from the front $\widetilde{\zeta}$ frequencies $\widetilde{\mathcal{X}}^{\widetilde{\zeta}}$.
Extract two-dimensional features $\alpha_P$ and $\theta_P$ using Eq. (22), (23).
Establish the GFN membership function model for magnitude $f_P^\alpha$ and phase $f_P^\theta$ using Eq. (28)-(33).
Choose a test sample $\{\hat{x}^1, \ldots, \hat{x}^k, \ldots, \hat{x}^K\}$.
Transform test sample to frequency domain $\left\{\widetilde{\hat{x}}^{\widetilde{k}}\right\}_{\widetilde{k}=1}^{\widetilde{K}}$ using Eq. (35).
Select values $\left\{\widetilde{\hat{x}}^{\widetilde{k}}\right\}_{\widetilde{k}=\widetilde{1}}^{\widetilde{\zeta}}$ from the front $\widetilde{\zeta}$ frequencies using Eq. (36).
Initialization: $\mathcal{Q} = \{\,\}$;
for $\widetilde{k} = \widetilde{1} : \widetilde{\zeta}$ do
    Obtain $\mathcal{F}_P^{\widetilde{k}\alpha}$ and $\mathcal{F}_P^{\widetilde{k}\theta}$ using Eq. (37).
    Obtain CDGFNs $\mathcal{F}_P^{\widetilde{k}}$ using Eq. (38), (39).
    Sort elements in $\mathcal{F}_P^{\widetilde{k}}$ in descending order based on square of their modulus using Eq. (40).
    Assign the sorted elements of $\mathcal{F}_P^{\widetilde{k}}$ to obtain membership degrees $\mathcal{M}^{\widetilde{k}}$ using Eq. (41), (42).
    Normalize $\mathcal{M}^{\widetilde{k}}$ to construct QBPA $\mathbb{Q}_{\mathbb{M}_{\widetilde{k}}}$ for frequency $\widetilde{k}$ using Eq. (43), (44).
    Append $\mathbb{Q}_{\mathbb{M}_{\widetilde{k}}}$ into $\mathcal{Q}$.
end for
Fuse QBPAs in $\mathcal{Q}$ to get combined QBPD $\mathbf{M}$ using Eq. (46).
Transform $\mathbf{M}$ into quantum pignistic probabilities $BetQP$ using Eq. (47).
Return predicted class index $\delta$ using Eq. (48).
```

E. CDGFN-MSIF Decision-Making Algorithm

Assume that $\widetilde{\zeta}$ sets of QBPA are generated with method described in Section IV-D, denoted as

$$\mathcal{Q} = \left\{\mathbb{Q}_{\mathbb{M}_{\widetilde{1}}}, \mathbb{Q}_{\mathbb{M}_{\widetilde{2}}}, \ldots, \mathbb{Q}_{\mathbb{M}_{\widetilde{k}}}, \ldots, \mathbb{Q}_{\mathbb{M}_{\widetilde{\zeta}}}\right\}. \tag{45}$$

Then, a CDGFN-MSIF algorithm for decision-making is then proposed as follows.

Step 1: The combined QBPD $\mathbf{M}$ (Definition 3) is obtained by fusing the $\widetilde{\zeta}$ sets of QBPA $\left\{\mathbb{Q}_{\mathbb{M}_{\widetilde{k}}}\right\}_{\widetilde{k}=1}^{\widetilde{\zeta}}$ with (11), represented as

$$\mathbf{M} = \mathbb{Q}_{\mathbb{M}_{\widetilde{1}}} \oplus \mathbb{Q}_{\mathbb{M}_{\widetilde{2}}} \cdots \oplus \mathbb{Q}_{\mathbb{M}_{\widetilde{k}}} \cdots \oplus \mathbb{Q}_{\mathbb{M}_{\widetilde{\zeta}}}. \tag{46}$$

Step 2: With (13) applying to $\mathbf{M}$, a set of quantum pignistic probabilities $BetQP$ assigned to singleton is obtained

$$BetQP = \{BetQP(\mathcal{W}_1), \ldots, BetQP(\mathcal{W}_p), \ldots, BetQP(\mathcal{W}_P)\} \tag{47}$$

Step 3: Finally, the class index δ with the highest $BetQP(\mathcal{W}_p)$ is selected

$$\delta = \arg\max_{1 \le p \le P}(BetQP(\mathcal{W}_p)). \tag{48}$$

Consequently, the proposition $\mathcal{W}_\delta$ is the predicted class.

The CDGFN-MSIF algorithm depends on generating QBPA for its decision-making process. Thus, a pseudocode of the whole process to make decision is described in Algorithm 1. It begins by transforming the training dataset into the frequency domain using DFT. From this, the most informative frequencies are selected based on TFI $\widetilde{\zeta}$, enabling the extraction of two-dimensional features. These features are used to establish GFN membership functions f_P^α and f_P^θ, which model uncertainty. For the testing phase, each test sample is similarly transformed into the frequency domain, with its selected frequency components processed through the GFN models to calculate the CDGFN $\mathcal{F}_P^{\widetilde{k}}$. These CDGFNs are utilized to generate QBPA $\mathbb{Q}_{\mathbb{M}_{\widetilde{k}}}$. The algorithm iteratively combines QBPAs $\left\{\mathbb{Q}_{\mathbb{M}_{\widetilde{k}}}\right\}_{\widetilde{k}=1}^{\widetilde{\zeta}}$ across all selected frequencies using the QECR, yielding a fused QBPD $\mathbf{M}$. Finally, the QBPD is converted into quantum pignistic probabilities $BetQP$, and the class with the highest probability δ is selected as the prediction.

V. EXPERIMENT

In this section, we apply the proposed method to some well-known time series classification datasets from UCR repository (https://archive.ics.uci.edu) and compare its accuracy to some state-of-the-art methods. Furthermore, we evaluate the effectiveness of the proposed design by conducting detailed ablation studies.

A. Experimental Setup

1) Compared Methods: We evaluate the proposed method CDGFN-MSIF (CM) against a range of classification techniques, categorized as evidence-theory-based, deep-learning-based, and machine-learning-based methods. Specifically, we compare the proposed method with two evidence-theory-based approaches: TFN-MSIF (TM) [64] and GFN-MSIF (GM) [65]. We also include four deep-learning-based methods: Multi-Layer Perceptron (MLP) [66], Multi-Scale Convolutional Neural Network (MCNN) [69], Time LeNet (t-LeNet) [70], and Multi-Channel Deep Convolutional Neural Network (MCDCNN) [71]. Additionally, four traditional machine-learning-based methods are evaluated: Decision Tree (DT) [79], Support Vector Machine (SVM) [80], AdaBoost (AB) [81], and Gradient Boosting (GB) [82].

2) Datasets: To evaluate the effectiveness of the proposed method, eight time series datasets from the UCR repository (https://archive.ics.uci.edu) are used, including Wafer, FordA,

TABLE II
OVERVIEW OF EXPERIMENTAL DATASETS

Dataset	*# Class*	*# SeqLen.*	*# Sample*
Wafer	2	152	7164
FordA	2	500	4921
FordB	2	500	4446
TwoLeadECG	2	82	1162
ECGFiveDays	2	136	884
WormsTwoClass	2	448	258
ToeSegmentation2	2	570	166
Coffee	2	286	56

FordB, TwoLeadECG, ECGFiveDays, WormsTwoClass, ToeSegmentation2, and Coffee. Summary details of these datasets are provided in Table II, with the number of classes (*# Class*), number of sequence length (*# SeqLen.*), and number of samples (*# Sample*).

3) Evaluation Details: For the accuracy calculation, a ten-fold cross-validation approach is used to derive the reported accuracy of all the methods on all datasets. Specifically, each dataset is split into ten equal segments. In each experiment, one segment (10%) is set aside as the testing group, while the remaining segments (90%) collectively form the training group. The accuracy scores from each iteration are recorded. Finally, the average accuracy, obtained through ten distinct tests, serves as the reported accuracy for a given dataset. However, for the four deep-learning-based methods (MLP [66], MCNN [69], t-LeNet [70], and MCDCNN [71]), the accuracy results were borrowed from [66], which also used ten-fold cross-validation. Further details on these methods are available in [66].

4) Selection of Threshold Frequency Index (TFI) $\widetilde{\zeta}$: In this experiment, the upper bound of TFI $\widetilde{\zeta}$ is set to $\frac{\widetilde{K}}{2}$, half of the time series length of the corresponding time series datasets. This setting reduces computation complexity and help to extract useful features. Therefore, to obtain one accuracy score out of ten tests in a ten-fold cross-validation for a dataset, we start the enumeration at $\widetilde{\zeta} = \widetilde{2}$ to ensure the acquired information is obtained from different sources (frequencies), which guarantees that the problem can be solved under the framework of QET. We end the enumeration at $\widetilde{\zeta} = \frac{\widetilde{K}}{2}$ to reduce redundant computation and increase the credibility of extracted features. For each TFI value, we apply the proposed method to execute the classification task. Throughout this iterative process, we record the accuracy score for each TFI value. Subsequently, the highest accuracy obtained during the enumeration of TFI $\widetilde{\zeta}$ is designated as the final accuracy score, while the corresponding TFI $\widetilde{\zeta}$ is selected as the optimal TFI.

B. Analysis

1) Comparison: The classification accuracy results for various methods are presented in Table III, with the highest performances highlighted in bold. The "Avg" column represents the mean accuracy for each method, while the row highlighted in orange indicates the performance of the proposed CDGFN-MSIF (CM) method. To make the comparison more intuitive and visually distinguishable, the results are also depicted in Fig. 4, with error bars displayed. The accuracy of proposed method is highlighted using horizontal line. The proposed method CM demonstrates superior classification performance, achieving the best results across six out of eight datasets: FordA (80.54%), FordB (80.37%), ECGFiveDays (100.00%), WormsTwoClass (72.36%), ToeSegmentation2 (83.63%), and Coffee (100.00%). In comparison, existing methods often perform poorly on these datasets. For instance, SVM achieves 80.12% accuracy on FordA but falls short on datasets like Coffee (51.82%), while deep-learning-based methods such as MCDCNN show variability, reaching 99.20% on Coffee but only 57.00% on WormsTwoClass. Additionally, the proposed method exhibits strong average performance across all datasets, achieving an average accuracy (Avg) of 88.15%, surpassing other evidence-theory-based methods such as GM (66.14%) and TM (64.89%). CM also achieves a lower standard deviation (Std) of 10.01%, reflecting stable performance across diverse datasets.

Besides, the proposed method performs better across all datasets than the traditional evidence-theory-based methods GM and TM, with nearly 20% accuracy difference of the Avg column. This demonstrates that the extracted two-dimensional features can express uncertainty more comprehensively. Furthermore, the aligned frequency domain makes the extracted features more effective and representative.

Notably, all the deep-learning-based methods struggle to perform effectively on these datasets listed in Table II. A possible reason for the relatively poor performance of deep learning models is the limited number of samples in these datasets. Deep learning methods typically require larger datasets to fully capture complex patterns, which may not be feasible in this case. Especially on small datasets like Coffee (56 samples), WormsTwoClass (258 samples), and ToeSegmentation2 (166 samples), the proposed method CM achieves exceptional results, with 100.00% accuracy on Coffee and 72.13% on WormsTwoClass, outperforming MCDCNN and MCNN, which reach only 57.00% and 50.00%, respectively. This finding emphasizes the strength of the proposed method, which is strongly suitable for scenarios with restricted data availability.

2) Ablation Study: Table IV presents the ablation study of critical design choices, with the highest accuracy are highlighted in bold. In *W/o feature selection*, we remove the TFI $\widetilde{\zeta}$, thereby extracting features from the entire frequency range. In *W/o CDGFN*, the GFN membership degrees of magnitude and phase of the original CDGFN at each frequency form separate real-valued CDGFNs, without the phase term.

As shown in Table IV, Without CDGFN, the model's performance drops notably, with an average accuracy of 80.15% compared to 88.19% in the full model, indicating that CDGFN effectively captures two-dimensional information, particularly through its complex-valued structure. Since CDGFN is the carrier of QBPA, this complex-valued nature leverages the constructive interference property in the QECR (Definition 4) to enhance multi-source information fusion. The absence of frequency selection has an even larger impact, reducing the average accuracy to 72.80% and leading to severe drops on certain datasets, such as

TABLE III
PERFORMANCE COMPARISON OF DIFFERENT METHODS ON EIGHT TIME SERIES DATASETS

Method	Dataset								Avg
	Wafer	FordA	FordB	TwoLeadECG	ECGFiveDays	WormsTwoClass	ToeSegmentation2	Coffee	
DT	99.09% ± 0.24%	58.01% ± 1.36%	55.49% ± 1.06%	94.92% ± 1.04%	96.00% ± 1.92%	63.34% ± 2.30%	73.41% ± 7.76%	88.00% ± 0.00%	78.53% ± 3.07%
SVM	99.15% ± 0.12%	80.12% ± 0.67%	78.99% ± 4.42%	**98.62%** ± 0.97%	99.99% ± 0.94%	61.25% ± 2.58%	83.16% ± 5.53%	51.82% ± 9.00%	81.64% ± 2.45%
AB	98.99% ± 0.29%	58.04% ± 0.96%	55.15% ± 1.54%	94.81% ± 1.06%	96.11% ± 1.34%	62.02% ± 2.62%	74.30% ± 7.17%	90.12% ± 9.02%	78.69% ± 2.99%
GB	99.15% ± 0.09%	60.76% ± 1.24%	61.35% ± 3.38%	98.06% ± 0.81%	99.10% ± 1.08%	61.22% ± 4.57%	78.40% ± 7.75%	92.30% ± 3.20%	81.29% ± 3.20%
MLP	**99.60%** ± 0.00%	73.00% ± 0.40%	60.30% ± 0.30%	76.20% ± 1.30%	97.00% ± 0.50%	60.10% ± 1.50%	74.50% ± 1.90%	99.60% ± 1.10%	80.04% ± 0.88%
MCNN	91.30% ± 4.40%	51.30% ± 0.40%	49.80% ± 1.20%	50.00% ± 0.00%	49.90% ± 0.30%	57.10% ± 0.00%	63.20% ± 30.90%	51.40% ± 3.50%	58.00% ± 5.04%
t-LeNet	89.20% ± 0.00%	51.00% ± 0.80%	51.20% ± 0.00%	50.00% ± 0.00%	49.70% ± 0.00%	55.70% ± 4.50%	81.50% ± 0.00%	53.60% ± 0.00%	60.24% ± 0.66%
MCDCNN	99.20% ± 0.30%	79.50% ± 2.60%	53.30% ± 2.90%	76.00% ± 16.80%	76.20% ± 13.40%	57.00% ± 0.00%	44.30% ± 15.20%	98.20% ± 2.50%	72.96% ± 6.95%
GM	64.93% ± 0.22%	49.61% ± 0.97%	51.09% ± 1.06%	70.81% ± 1.27%	86.97% ± 0.86%	42.40% ± 4.32%	69.77% ± 3.30%	93.52% ± 2.77%	66.36% ± 1.35%
TM	89.00% ± 0.57%	47.80% ± 0.64%	48.13% ± 0.98%	79.13% ± 1.22%	83.66% ± 0.72%	42.25% ± 2.20%	75.48% ± 3.30%	53.67% ± 6.32%	64.94% ± 1.72%
CM	99.16% ± 0.08%	**80.54%** ± 0.34%	**80.37%** ± 0.52%	89.54% ± 0.77%	**100.00%** ± 0.00%	**72.36%** ± 2.09%	**83.63%** ± 2.72%	**100.00%** ± 0.00%	**88.19%** ± 0.82%

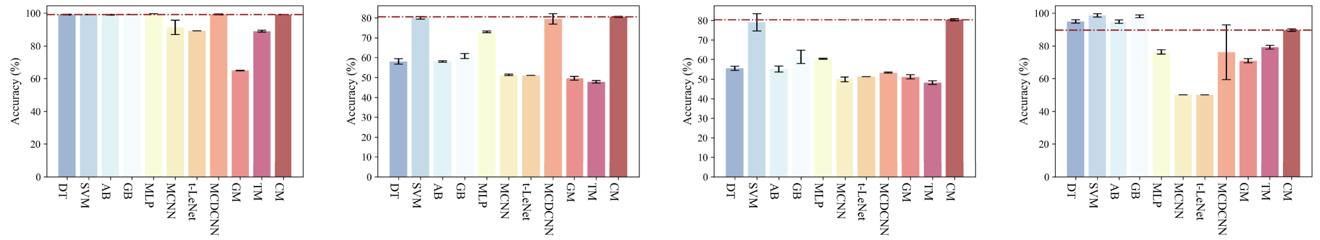

(a) Wafer (b) FordA (c) FordB (d) TwoLeadECG

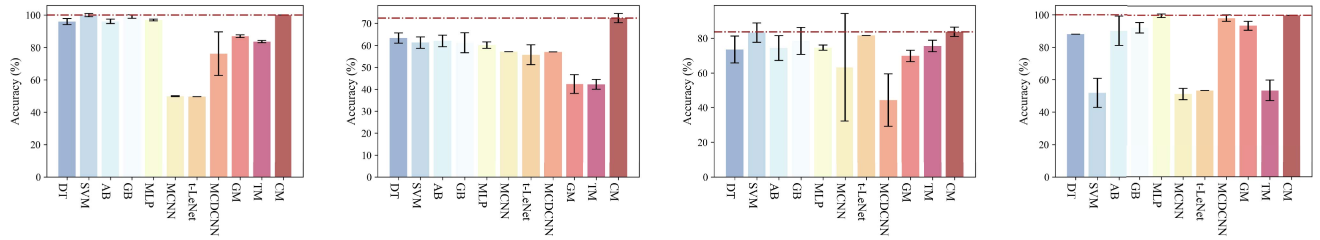

(e) ECGFiveDays (f) WormsTwoClass (g) ToeSegmentation2 (h) Coffee

Fig. 4. Accuracy comparison of different methods across eight time series datasets.

TABLE IV
ABLATION STUDY OF CRITICAL DESIGN CHOICES

Dataset	W/o frequency selection	W/o CDGFN	CM
Wafer	98.35% ± 0.13%	91.82% ± 0.16%	**99.16%** ± 0.08%
FordA	61.83% ± 1.00%	71.14% ± 0.64%	**80.54%** ± 0.34%
FordB	63.37% ± 0.78%	76.15% ± 0.57%	**80.37%** ± 0.52%
TwoLeadECG	73.00% ± 0.94%	81.22% ± 1.30%	**89.54%** ± 0.77%
ECGFiveDays	99.98% ± 0.05%	90.63% ± 0.64%	**100.00%** ± 0.00%
WormsTwoClass	60.85% ± 0.75%	64.65% ± 3.18%	**72.26%** ± 2.09%
ToeSegmentation2	27.13% ± 3.64%	67.71% ± 5.27%	**83.63%** ± 2.72%
Coffee	97.88% ± 2.08%	97.91% ± 1.98%	**100.00%** ± 0.00%
Avg	72.80% ± 1.17%	80.15% ± 1.72%	**88.19%** ± 0.82%

FordA and ToeSegmentation2. This demonstrates that selecting the features at the front frequencies can greatly improve the credibility of extracted features. Overall, these findings confirm that both components significantly improve model performance across diverse datasets.

3) The Value of Optimal TFI: In the ablation study, we observe that the TFI $\widetilde{\zeta}$ has a huge impact on the proposed CDGFN-MSIF method. However, we still want to determine whether the optimal TFI is located within the lower (or "front") frequency range, as we described in the feature extraction section. We examined the results shown in Fig. 5. Each subplot illustrates how classification accuracy changes across a range of optimal TFI values for various datasets, from $\widetilde{0}$ to $\widetilde{K}$ in increments of $\widetilde{\frac{K}{20}}$, where $\widetilde{K}$ represents the length of the frequency space for each dataset.

From the figure, we can see that the highest accuracy, or optimal TFI, is often achieved when selecting features from the front frequencies, while increasing optimal TFI to include higher frequencies generally leads to a drop in accuracy. This trend is especially evident in datasets like FordA, FordB, TwoLeadECG, and ToeSegmentation2, where accuracy peaks at low optimal TFI values and declines as higher frequencies are included. For datasets like Wafer, ECGFiveDays, and Coffee, accuracy remains stable across optimal TFI values, but including only the front frequencies is still sufficient to achieve near-optimal accuracy. This result suggests that high-frequency components are largely uninformative for these time series datasets, reinforcing the effectiveness of the proposed method to only focus on lower-frequency information.

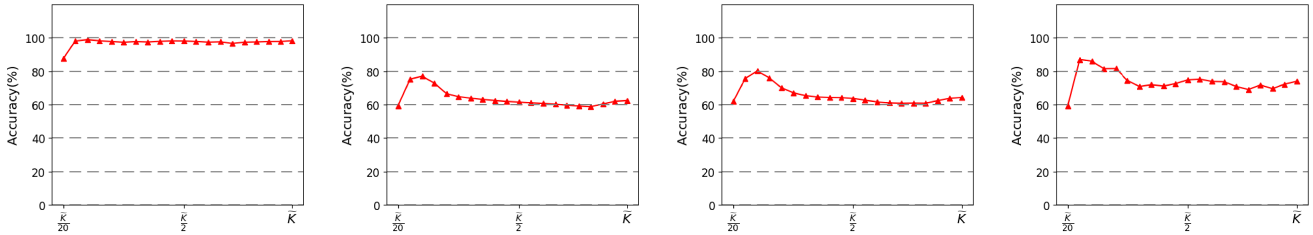

(a) Wafer (b) FordA (c) FordB (d) TwoLeadECG

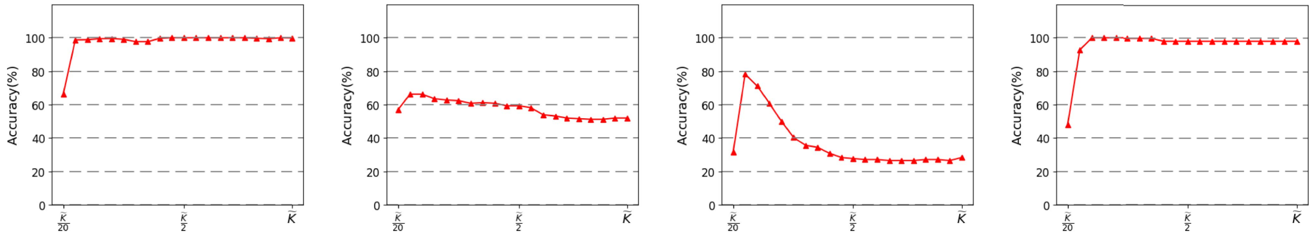

(e) ECGFiveDays (f) WormsTwoClass (g) ToeSegmentation2 (h) Coffee

Fig. 5. The effect of the optimal TFI $\widetilde{\zeta}$ on classification accuracy for the eight time series datasets.

TABLE V
OPTIMAL TFI VALUES AND THEIR RATIOS TO TOTAL SEQUENCE LENGTHS ACROSS DATASETS.

Dataset	Optimal TFI Value	*# SeqLen.*	*Ratio*
Wafer	16	152	10.53%
FordA	39	500	7.80%
FordB	51	500	10.20%
TwoLeadECG	8	82	9.76%
ECGFivedays	66	136	48.53%
WormsTwoClass	23	900	2.56%
ToeSegmentation2	16	343	4.66%
Coffee	27	286	9.44%

TABLE VI
COMPARISON OF ACCURACY USING HILBERT AND DFT TRANSFORMATIONS

Dataset	CM (Hilbert)	CM (DFT)
Wafer	92.80% ± 1.15%	**99.16%** ± 0.08%
FordA	53.10% ± 1.98%	**80.54%** ± 0.34%
FordB	51.89% ± 0.81%	**80.37%** ± 0.52%
TwoLeadECG	84.59% ± 1.71%	**89.54%** ± 0.77%
ECGFiveDays	62.21% ± 3.05%	**100.00%** ± 0.00%
WormsTwoClass	58.54% ± 3.57%	**72.26%** ± 2.09%
ToeSegmentation2	68.63% ± 5.81%	**83.63%** ± 2.72%
Coffee	85.61% ± 7.39%	**100.00%** ± 0.00%
Avg	69.67% ± 3.18%	**88.19%** ± 0.82%

Additionally, we also present the optimal TFI values and their ratios to the sequence length in Table V. Here, the *Ratio* indicates the percentage obtained by dividing the optimal TFI value by the sequence length (*# SeqLen.*) for each dataset. As observed, all optimal TFI values are concentrated within the first 10% of the total sequence length, with the exception of the ECGFiveDays dataset. However, the accuracy for ECGFiveDays remains consistently close to 100.00% at the front frequencies, as shown in Fig. 5(e). Therefore, in practical applications, the upper bound of the TFI can be controlled within 10%-20% of the total sequence length. This setting can ensure high accuracy while significantly reducing the computational complexity of the enumeration process.

4) Validation of Selection of Discrete Fourier Transform (DFT): To validate the choice for selecting DFT for converting time-domain data to the frequency domain, we compared its performance with the Hilbert transform (Hilbert) [83] as shown in Table VI. DFT consistently achieved higher accuracy across all datasets. For example, DFT reached 99.16% accuracy on the Wafer dataset, compared to 92.80% with Hilbert. On average, DFT provided 88.19% accuracy versus 69.67% for Hilbert, confirming DFT as the more effective and stable transformation for the proposed approach. These results suggest that choosing an effective frequency domain transformation method can significantly enhance performance. This insight motivates future exploration of advanced transformation techniques specifically tailored for time series data.

5) Computational Complexity Analysis: It is worth noting that in this subsection, the notation $\mathcal{O}$ denotes the asymptotic time complexity (Big-O notation), which is distinct from the feature proxy $\mathcal{O}$ defined in Definition 9. The computational complexity of the proposed CDGFN-MSIF algorithm is primarily determined by two stages: feature extraction and decision-making. In the feature extraction stage, the DFT is employed, which consumes $\mathcal{O}(K \log K)$ for a time series sequence of length K. Subsequently, the generation of QBPA across the selected threshold frequency index $\widetilde{\zeta}$ for P classes operates with a complexity of $\mathcal{O}(\widetilde{\zeta} \cdot 2^P)$, as it involves assigning probability values to the power set of the frame of discernment. The decision-making stage, which utilizes the QECR to fuse evidence from $\widetilde{\zeta}$ sources, involves the intersection of focal elements in the power set, resulting in a complexity of $\mathcal{O}(\widetilde{\zeta} \cdot 2^{2P})$. Consequently, the overall time complexity for classifying a single test instance is approximately $\mathcal{O}(K \log K + \widetilde{\zeta} \cdot 2^{2P})$. Since the optimal TFI $\widetilde{\zeta}$ is typically a small fraction of K and the number of classes P is limited in standard TSC tasks, the proposed method remains computationally efficient and scalable compared to deep learning-based approaches that require computationally intensive iterative training.

VI. CONCLUSION

Time series classification has always been an important topic in practical application, and this paper presents a novel method for constructing QBPA to apply QET to one-dimensional TSC task. The proposed method emphasizes extracting informative features from the front-few multi-frequency components of the aligned frequency domain, achieved by setting a TFI to limit the range of frequencies considered. By leveraging the DFT and introducing the CDGFN for two-dimensional uncertainty representation, the proposed approach constructs QBPA to comprehensively represent information of the front-few frequency components. The CDGFN-MSIF algorithm then effectively fuses these QBPAs to reason uncertainty, resulting in superior performance compared to state-of-the-art methods, particularly in datasets with varying sizes. This demonstrates the robustness and effectiveness of the proposed approach in diverse TSC scenarios. Beyond standard benchmarks, this method holds significant potential for applications involving periodic signals, such as rotating machinery fault diagnosis and physiological signal monitoring (e.g., EEG/ECG [84]), where frequency-domain features are intrinsically significant.

While these results are encouraging, several limitations need further investigation. One is to apply the proposed method to multivariate time series classification task. Analyzing different variables in the multivariate time series data as an additional layer of evidence source indicates the promise of this research. Another focus should be developing higher-quality techniques to transform time-domain data into the frequency domain, which would enhance the quality of extracted features and likely improve performance. Finally, leveraging the finding that effective features are mostly low-frequency, we aim to develop an adaptive mechanism to automatically select the optimal TFI, thereby streamlining the feature extraction process and avoiding exhaustive enumeration.

ACKNOWLEDGMENT

The authors would like to thank the editor and anonymous reviewers for their valuable feedback and insightful suggestions, which have significantly enhanced the quality of this article. The experimental and computational work in this research run on the Huawei Cloud AI Compute Service. The authors appreciate the stable compute supply from this platform.

REFERENCES

[1] H. Zhang, Y.-F. Zhang, Z. Zhang, Q. Wen, and L. Wang, “LogoRA: Local-global representation alignment for robust time series classification,” *IEEE Trans. Knowl. Data Eng.*, vol. 36, no. 12, pp. 8718–8729, Dec. 2024.

[2] Q. Ma et al., “A survey on time-series pre-trained models,” *IEEE Trans. Knowl. Data Eng.*, vol. 36, no. 12, pp. 7536–7555, Dec. 2024.

[3] G. He, L. Dai, Z. Yu, and C. P. Chen, “GAN-based temporal association rule mining on multivariate time series data,” *IEEE Trans. Knowl. Data Eng.*, vol. 36, no. 10, pp. 5168–5180, Oct. 2024.

[4] G. He, D. Jin, L. Dai, X. Xin, Z. Yu, and C. P. Chen, “Online learning of temporal association rule on dynamic multivariate time series data,” *IEEE Trans. Knowl. Data Eng.*, vol. 36, no. 12, pp. 8954–8966, Dec. 2024.

[5] G. He et al., “Efficient semi-supervised clustering with pairwise constraint propagation for multivariate time series,” *Inf. Sci.*, vol. 681, 2024, Art. no. 121233.

[6] Q. Wen, L. Yang, T. Zhou, and L. Sun, “Robust time series analysis and applications: An industrial perspective,” in *Proc. 28th ACM SIGKDD Conf. Knowl. Discov. Data Mining*, 2022, pp. 4836–4837.

[7] N. S. Alghamdi, L. Zhang, E. A. Rundensteiner, and M. Y. Eltabakh, “Scalable time series compound infrastructure,” in *Proc. Int. Conf. Manage. Data*, 2022, pp. 1685–1698.

[8] E. Ramanujam, T. Perumal, and S. Padmavathi, “Human activity recognition with smartphone and wearable sensors using deep learning techniques: A review,” *IEEE Sensors J.*, vol. 21, no. 12, pp. 13029–13040, Jun. 2021.

[9] H. Xu, Y. Wang, S. Jian, Q. Liao, Y. Wang, and G. Pang, “Calibrated one-class classification for unsupervised time series anomaly detection,” *IEEE Trans. Knowl. Data Eng.*, vol. 36, no. 11, pp. 5723–5736, Nov. 2024.

[10] Z. Zhong, Z. Yu, Z. Fan, C. P. Chen, and K. Yang, “Adaptive memory broad learning system for unsupervised time series anomaly detection,” *IEEE Trans. Neural Netw. Learn. Syst.*, vol. 36, no. 5, pp. 8331–8345, May 2024.

[11] L. Sun, M. Zhang, B. Wang, and P. Tiwari, “Few-shot class-incremental learning for medical time series classification,” *IEEE J. Biomed. Health Informat.*, vol. 28, no. 4, pp. 1872–1882, Apr. 2024.

[12] L. Zhang and F. Xiao, “Belief Rényi divergence of divergence and its application in time series classification,” *IEEE Trans. Knowl. Data Eng.*, vol. 36, no. 8, pp. 3670–3681, Aug. 2024.

[13] R. Liu, T. Xiahou, and Y. Liu, “Multisource imprecise information calibration for reliability assessment of multistate systems: A consensus reaching perspective,” *IEEE Trans. Rel.*, vol. 74, no. 1, pp. 2226–2240, Jan. 2025.

[14] Z. Zhang, Z. Liu, H. Tian, and A. Martin, “Mixed-type imputation for missing data credal classification via quality matrices,” *IEEE Trans. Syst., Man, Cybern. Syst.*, vol. 54, no. 8, pp. 4772–4785, Aug. 2024.

[15] W. Zhang, Z. Deng, T. Zhang, K.-S. Choi, and S. Wang, “Multi-view fuzzy representation learning with rules based model,” *IEEE Trans. Knowl. Data Eng.*, vol. 36, no. 2, pp. 736–749, Feb. 2024.

[16] T. Zhan, J. Zhou, Z. Li, and Y. Deng, “Generalized information entropy and generalized information dimension,” *Chaos, Solitons Fractals*, vol. 184, 2024, Art. no. 114976.

[17] Z.-G. Liu, Y.-M. Fu, Q. Pan, and Z.-W. Zhang, “Orientational distribution learning with hierarchical spatial attention for open set recognition,” *IEEE Trans. Pattern Anal. Mach. Intell.*, vol. 45, no. 7, pp. 8757–8772, Jul. 2023.

[18] D. Meng, S. Yang, A. M. de Jesus, and S.-P. Zhu, “A novel Kriging-model-assisted reliability-based multidisciplinary design optimization strategy and its application in the offshore wind turbine tower,” *Renewable Energy*, vol. 203, pp. 407–420, 2023.

[19] D. Meng, S. Yang, A. M. De Jesus, T. Fazeres-Ferradosa, and S.-P. Zhu, “A novel hybrid adaptive kriging and water cycle algorithm for reliability-based design and optimization strategy: Application in offshore wind turbine monopile,” *Comput. Methods Appl. Mechan. Eng.*, vol. 412, 2023, Art. no. 116083.

[20] P. Liu, X. Wang, Y. Fu, and P. Wang, “Graph model for conflict resolution for mixed-stability combinatorial foresight based on the combination of regret theory and VIKOR method,” *IEEE Trans. Fuzzy Syst.*, vol. 32, no. 11, pp. 6486–6499, Nov. 2024.

[21] S. Xia et al., “An efficient and accurate rough set for feature selection, classification, and knowledge representation,” *IEEE Trans. Knowl. Data Eng.*, vol. 35, no. 8, pp. 7724–7735, Aug. 2023.

[22] X. Deng and W. Jiang, “A framework for the fusion of non-exclusive and incomplete information on the basis of d number theory,” *Appl. Intell.*, vol. 53, pp. 11861–11884, 2023.

[23] Z. Wang, L. Wang, A. Szolnoki, and M. Perc, “Evolutionary games on multilayer networks: A colloquium,” *Eur. Phys. J. B*, vol. 88, pp. 1–15, 2015.

[24] Z. Wang, S. Kokubo, M. Jusup, and J. Tanimoto, “Universal scaling for the dilemma strength in evolutionary games,” *Phys. Life Rev.*, vol. 14, pp. 1–30, 2015.

[25] A. P. Dempster, “Upper and lower probabilities generated by a random closed interval,” *Ann. Math. Statist.*, vol. 39, pp. 957–966, 1968.

[26] G. Shafer, *A Mathematical Theory of Evidence*, vol. 42. Princeton, NJ, USA: Princeton Univ. Press, 1976.

[27] Z. Wang, C. Mu, S. Hu, C. Chu, and X. Li, “Modelling the dynamics of regret minimization in large agent populations: A master equation approach,” in *Proc. Int. Joint Conf. Artif. Intell.*, 2022, pp. 534–540.

[28] Z. Wang, M. Jusup, L. Shi, J.-H. Lee, Y. Iwasa, and S. Boccaletti, “Exploiting a cognitive bias promotes cooperation in social dilemma experiments,” *Nature Commun.*, vol. 9, no. 1, 2018, Art. no. 2954.

[29] Z. Wang et al., “Onymity promotes cooperation in social dilemma experiments,” *Sci. Adv.*, vol. 3, no. 3, 2017, Art. no. e1601444.

[30] X. Li et al., “Punishment diminishes the benefits of network reciprocity in social dilemma experiments,” *Proc. Nat. Acad. Sci.*, vol. 115, no. 1, pp. 30–35, 2018.

[31] R. R. Yager, “On the fusion of imprecise uncertainty measures using belief structures,” *Inf. Sci.*, vol. 181, no. 15, pp. 3199–3209, 2011.

[32] D.-V. Vo, T.-T. Tran, K. Shirai, and V.-N. Huynh, “Deep generative networks coupled with evidential reasoning for dynamic user preferences using short texts,” *IEEE Trans. Knowl. Data Eng.*, vol. 35, no. 7, pp. 6811–6826, Jul. 2023.

[33] J.-B. Yang and D.-L. Xu, “Maximum likelihood evidential reasoning,” *Artif. Intell.*, vol. 340, 2025, Art. no. 104289.

[34] L. Chang, L. Zhang, C. Fu, and Y.-W. Chen, “Transparent digital twin for output control using belief rule base,” *IEEE Trans. Cybern.*, vol. 52, no. 10, pp. 10364–10378, Oct. 2022.

[35] F. Xiao, J. Wen, W. Pedrycz, and M. Aritsugi, “Complex evidence theory for multisource data fusion,” *Chin. J. Inf. Fusion*, vol. 1, no. 2, pp. 134–159, 2024.

[36] Y. Deng, “Random permutation set,” *Int. J. Comput. Commun. Control*, vol. 17, no. 1, 2022, Art. no. 4542.

[37] X. Su, X. Chen, H. Qian, and C. Jiang, “BDOS: An orthogonal sum based on belief of permutation events and element distances in random permutation set,” *Expert Syst. Appl.*, vol. 298, 2026, Art. no. 129513.

[38] J. Deng, Y. Deng, and J.-B. Yang, “Random permutation set reasoning,” *IEEE Trans. Pattern Anal. Mach. Intell.*, vol. 46, no. 12, pp. 10246–10258, Dec. 2024.

[39] Q. Zhou, W. Pedrycz, and Y. Deng, “Order-2 probabilistic information fusion on random permutation set,” *IEEE Trans. Knowl. Data Eng.*, vol. 37, no. 2, pp. 837–850, Feb. 2025.

[40] Y. Wang, Z. Li, and Y. Deng, “A new orthogonal sum in random permutation set,” *Fuzzy Sets Syst.*, vol. 490, 2024, Art. no. 109034.

[41] Y. Huang, F. Xiao, Z. Cao, and C.-T. Lin, “Higher order fractal belief Rényi divergence with its applications in pattern classification,” *IEEE Trans. Pattern Anal. Mach. Intell.*, vol. 45, no. 12, pp. 14709–14726, Dec. 2023.

[42] Y. Huang, F. Xiao, Z. Cao, and C.-T. Lin, “Fractal belief Rényi divergence with its applications in pattern classification,” *IEEE Trans. Knowl. Data Eng.*, vol. 36, no. 12, pp. 8297–8312, Dec. 2024.

[43] F. Xiao, W. Ding, and W. Pedrycz, “A generalized f-divergence with applications in pattern classification,” *IEEE Trans. Knowl. Data Eng.*, vol. 37, no. 4, pp. 1556–1570, Apr. 2025, doi: 10.1109/TKDE.2025.3530524.

[44] T. Zhao, Z. Li, and Y. Deng, “Linearity in Deng entropy,” *Chaos, Solitons Fractals*, vol. 178, 2024, Art. no. 114388.

[45] X. Su, J. Zhong, Z. Hong, H. Qian, and D. Pelusi, “A novel belief entropy and its application in cooperative situational awareness,” *Expert Syst. Appl.*, vol. 286, 2025, Art. no. 128027, doi: 10.1016/j.eswa.2025.128027.

[46] D. Han, J. Dezert, and Y. Yang, “Belief interval-based distance measures in the theory of belief functions,” *IEEE Trans. Syst., Man, Cybern. Syst.*, vol. 48, no. 6, pp. 833–850, Jun. 2018.

[47] C. Qiang, Y. Deng, and K. H. Cheong, “Information fractal dimension of mass function,” *Fractals*, vol. 30, 2022, Art. no. 2250110.

[48] L. Zhu, Q. Zhou, Y. Deng, and K. H. Cheong, “Fractal-based basic probability assignment: A transient mass function,” *Inf. Sci.*, vol. 652, 2024, Art. no. 119767.

[49] Z. Zhou, G. Hu, C. Hu, C. Wen, and L. Chang, “A survey of belief rule-base expert system,” *IEEE Trans. Syst., Man, Cybern. Syst.*, vol. 51, no. 8, pp. 4944–4958, Aug. 2021.

[50] T. Xiahou, Z. Zeng, and Y. Liu, “Remaining useful life prediction by fusing expert knowledge and condition monitoring information,” *IEEE Trans. Ind. Informat.*, vol. 17, no. 4, pp. 2653–2663, Apr. 2021.

[51] X. Fan, M. Zhou, B. Cheng, J. Wu, and H. Fujita, “Two-stage heterogeneous noncooperative behavior for consensus in large-scale group decision under fuzzy distributed preference relation,” *IEEE Trans. Fuzzy Syst.*, vol. 33, no. 11, pp. 4003–4016, Nov. 2025.

[52] L. Ni, Y.-W. Chen, and O. de Brujin, “Towards understanding socially influenced vaccination decision making: An integrated model of multiple criteria belief modelling and social network analysis,” *Eur. J. Oper. Res.*, vol. 293, no. 1, pp. 276–289, 2021.

[53] Y.-J. Zhou, M. Zhou, J. Wu, W. Pedrycz, and X.-B. Liu, “Asynchronous consensus evolution mechanism for large group emergency decision making: Risk mitigation strategy selection under uncertainty,” *IEEE Trans. Syst., Man, Cybern. Syst.*, vol. 55, no. 10, pp. 6753–6766, Oct. 2025.

[54] L. Fei and Y. Wang, “An optimization model for rescuer assignments under an uncertain environment by using Dempster–Shafer theory,” *Knowl.-Based Syst.*, vol. 255, 2022, Art. no. 109680.

[55] X. Chen and Y. Deng, “Evidential software risk assessment model on ordered frame of discernment,” *Expert Syst. Appl.*, vol. 250, 2024, Art. no. 123786.

[56] X. Su, X. Huang, X. Pan, and D. Meng, “A dependence assessment method based on quantum model of mass function in human reliability analysis,” *Expert Syst. Appl.*, vol. 299, 2026, Art. no. 129992.

[57] Z.-W. Zhang, Z.-G. Liu, A. Martin, and K. Zhou, “BSC: Belief shift clustering,” *IEEE Trans. Syst., Man, Cybern. Syst.*, vol. 53, no. 3, pp. 1748–1760, Mar. 2023.

[58] Z. Zhang, H. Tian, J. Zuo, and W. Ding, “Aggregation-based self-supervised evidential clustering for imbalanced data,” *Inf. Fusion*, vol. 127, 2026, Art. no. 103721.

[59] L. Fei, X. Liu, and C. Zhang, “An evidential linguistic ELECTRE method for selection of emergency shelter sites,” *Artif. Intell. Rev.*, vol. 57, no. 4, 2024, Art. no. 81.

[60] P. Schäfer and M. Högqvist, “SFA: A symbolic fourier approximation and index for similarity search in high dimensional datasets,” in *Proc. 15th Int. Conf. Extending Database Technol.*, New York, NY, USA, 2012, pp. 516–527.

[61] F. Xiao, “Quantum evidence theory,” 2025, *viXra:2504.0202*.

[62] F. Xiao, “Quantum X-entropy in generalized quantum evidence theory,” *Inf. Sci.*, vol. 643, 2023, Art. no. 119177.

[63] F. Xiao, Y. Zhou, and W. Pedrycz, “An adaptive quantum circuit of Dempster’s rule of combination for uncertain pattern classification,” in *Proc. 39th Neural Inf. Process. Syst. Annu. Conf.*, 2025, pp. 1–14.

[64] W. Jiang, D. Duanmu, X. Fan, and Y. Deng, “A new method to determine basic probability assignment under fuzzy environment,” in *Proc. Int. Conf. Syst. Informat.*, 2012, pp. 758–762.

[65] Y. Zhang, W. Jiang, and X. Deng, “Fault diagnosis method based on time domain weighted data aggregation and information fusion,” *Int. J. Distrib. Sensor Netw.*, vol. 15, no. 9, 2019, Art. no. 1550147719875629.

[66] H. Ismail Fawaz, G. Forestier, J. Weber, L. Idoumghar, and P.-A. Muller, “Deep learning for time series classification: A review,” *Data Min. Knowl. Discov.*, vol. 33, no. 4, pp. 917–963, Jul. 2019.

[67] F. Wang et al., “Convolutional preprocessing transformer-based fault diagnosis for rectifier-filter circuits in nuclear power plants,” *Rel. Eng. Syst. Saf.*, vol. 249, 2024, Art. no. 110198.

[68] B. Cao, C. Li, Y. Song, Y. Qin, and C. Chen, “Network intrusion detection model based on CNN and GRU,” *Appl. Sci.*, vol. 12, no. 9, 2022, Art. no. 4184.

[69] Z. Cui, W. Chen, and Y. Chen, “Multi-scale convolutional neural networks for time series classification,” 2016, *arXiv:1603.06995*.

[70] A. Le Guennec, S. Malinowski, and R. Tavenard, “Data augmentation for time series classification using convolutional neural networks,” in *Proc. ECML/PKDD Workshop Adv. Analytics Learn. Temporal Data*, 2016, pp. 64–77.

[71] Y. Zheng, Q. Liu, E. Chen, Y. Ge, and J. L. Zhao, “Time series classification using multi-channels deep convolutional neural networks,” in *Proc. Int. Conf. Web-Age Inf. Manage.*, 2014, pp. 298–310.

[72] Q. Ma, L. Shen, W. Chen, J. Wang, J. Wei, and Z. Yu, “Functional echo state network for time series classification,” *Inf. Sci.*, vol. 373, pp. 1–20, 2016.

[73] K. Han, A. M. Koay, R. K. Ko, W. Chen, and M. Xu, “Adapting to the stream: An instance-attention GNN method for irregular multivariate time series data,” *Front. Comput. Sci.*, vol. 19, no. 8, 2025, Art. no. 198340.

[74] D. Sundararajan, *The Discrete Fourier Transform: Theory, Algorithms and Applications*. Singapore: World Scientific, 2001.

[75] D. Ramot, R. Milo, M. Friedman, and A. Kandel, “Complex fuzzy sets,” *IEEE Trans. Fuzzy Syst.*, vol. 10, no. 2, pp. 171–186, Apr. 2002.

[76] F.-P. Chan, A.-C. Fu, and C. Yu, “Haar wavelets for efficient similarity search of time-series: With and without time warping,” *IEEE Trans. Knowl. Data Eng.*, vol. 15, no. 3, pp. 686–705, May/Jun. 2003.

[77] W. Jiang, K. Huang, J. Geng, and X. Deng, “Multi-scale metric learning for few-shot learning,” *IEEE Trans. Circuits Syst. Video Technol.*, vol. 31, no. 3, pp. 1091–1102, Mar. 2021.

[78] X. Deng, S. Xue, and W. Jiang, “A novel quantum model of mass function for uncertain information fusion,” *Inf. Fusion*, vol. 89, pp. 619–631, 2023.

[79] J. R. Quinlan, “Learning decision tree classifiers,” *ACM Comput. Surv.*, vol. 28, no. 1, pp. 71–72, 1996.

[80] C. Cortes and V. Vapnik, “Support-vector networks,” *Mach. Learn.*, vol. 20, pp. 273–297, 1995.
[81] Y. Freund and R. E. Schapire, “A decision-theoretic generalization of on-line learning and an application to boosting,” *J. Comput. Syst. Sci.*, vol. 55, no. 1, pp. 119–139, Aug. 1997.
[82] J. H. Friedman, “Greedy function approximation: A gradient boosting machine,” *Ann. Stat.*, vol. 29, no. 5, pp. 1189–1232, Oct. 2001.
[83] V. Cizek, “Discrete Hilbert transform,” *IEEE Trans. Audio Electroacoust.*, vol. 18, no. 4, pp. 340–343, Apr. 1970.
[84] Z. Liu, F. Xiao, C.-T. Lin, and Z. Cao, “A robust evidential multisource data fusion approach based on cooperative game theory and its application in EEG,” *IEEE Trans. Syst., Man, Cybern. Syst.*, vol. 54, no. 2, pp. 729–740, Feb. 2024.

Junhao Yu is currently working toward the bachelor’s degree with the School of Big Data and Software Engineering, Chongqing University. He is currently an undergraduate student supervised by professor Fuyuan Xiao with the School of Big Data and Software Engineering, Chongqing University. His research interests include information fusion, and 3D reconstruction.

Fuyuan Xiao (Senior Member, IEEE) received the DE degree in computer science and communication engineering from the Graduate School of Science and Technology, Kumamoto University, Japan. She is a professor with the School of Big Data and Software Engineering, Chongqing University. She has published many papers in prestigious journals and conferences, including *IEEE Transactions on Pattern Analysis and Machine Intelligence*, *IEEE Transactions on Knowledge and Data Engineering*, *IEEE Transactions on Neural Networks and Learning Systems*, *IEEE Transactions on Cybernetics*, *IEEE Transactions on Fuzzy Systems*, and *IEEE Transactions on Systems, Man, and Cybernetics: Systems*. She also serves as a reviewer for several prestigious journals, such as *IEEE Transactions on Pattern Analysis and Machine Intelligence*, *IEEE Transactions on Knowledge and Data Engineering*, *IEEE Transactions on Neural Networks and Learning Systems*, *IEEE Transactions on Fuzzy Systems*, *IEEE Transactions on Cybernetics*, and *IEEE Internet of Things Journal*, etc. Her research interests include information fusion, trustworthy reasoning, and quantum artificial intelligence.

Yi Zhang received the PhD degree from Chongqing University, Chongqing, China, in 2001. He is currently a professor with the School of Big Data and Software Engineering, Chongqing University, China. He has authored more than 60 research papers in academic journals and conferences. His research has been supported by the National Natural Science Foundation of China, National Science and Technology Support Program, Chongqing Science and Technology Plan, Chongqing Natural Science Foundation, and Chongqing Key Projects. His research interests include software engineering, Big Data analytics, and artificial intelligence.

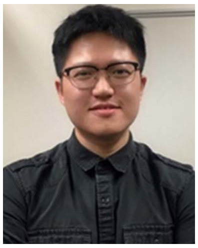

Zehong Cao (Senior Member, IEEE) received the PhD degree from the Australian AI Institute, University of Technology Sydney, in 2017 and has published more than 100 outputs in top-quality journals and conferences. He is an associate professor in AI and leads the research in human-agent interaction and learning with Adelaide University, Australia. His exceptional contributions have been recognised with prestigious awards and fellowships, such as being Australian Research Council (ARC) Discovery Early Career Researcher Award (DECRA) Fellowship (2022), Baidu AI Chinese Young Scholar (AI+X category, 2022), DAAD AInet Fellow (2022), ACM’s Distinguished Speaker (2022), Inaugural Enterprise Fellowship (2022), UniSA STEM Early-career Research Award (2022) and Mid-Career Reseach Award (2025), and Japan Society for the Promotion of Science (JSPS) Invitational Fellowship (2023). He serves as associate editor in various journals, such as *IEEE Transactions on Neural Networks and Learning Systems* and *IEEE Transactions on Fuzzy Systems*, and as area chairs for various conferences including AAMAS, KDD, MM, AAAI, IJCAI, and NeurIPS. His research interests encompass reinforcement learning, brain-computer interfaces, and decision-making.

Chin-Teng Lin (Fellow, IEEE) received the bachelor’s of science from National Chiao-Tung University (NCTU), Taiwan, in 1986, the master’s, and the PhD degrees in electrical engineering from Purdue University, USA, received in 1989 and 1992, respectively. He is currently a distinguished professor with School of Computer Science and co-director of the Australian Artificial Intelligence Institute (AAII) within the Faculty of Engineering and Information Technology, University of Technology Sydney, Australia. He is also an Honorary chair professor of electrical and computer engineering with NCTU. For his contributions to biologically inspired information systems, Prof Lin was awarded Fellowship with the IEEE, in 2005, and with the International Fuzzy Systems Association (IFSA), in 2012. He received the IEEE Fuzzy Systems Pioneer Award, in 2017 and the IEEE Lotfi A. Zadeh Award for Emerging Technologies, in 2026. He has held notable positions as editor-in-chief of IEEE Transactions on Fuzzy Systems from 2011 to 2016; seats on Board of Governors for the IEEE Circuits and Systems (CAS) Society (2005-2008), IEEE Systems, Man, Cybernetics (SMC) Society (2003-2005), IEEE Computational Intelligence Society (2008-2010); Chair of the IEEE Taipei Section (2009-2010); Chair of IEEE CIS Awards Committee (2022, 2023); Distinguished Lecturer with the IEEE CAS Society (2003-2005) and the CIS Society (2015-2017); Chair of the IEEE CIS Distinguished Lecturer Program Committee (2018-2019); Deputy Editor-in-Chief of IEEE Transactions on Circuits and Systems-II (2006-2008); Program Chair of the IEEE International Conference on Systems, Man, and Cybernetics (2005); and General Chair of the 2011 and 2027 IEEE International Conference on Fuzzy Systems. Prof Lin is the co-author of Neural Fuzzy Systems (Prentice-Hall) and the author of Neural Fuzzy Control Systems with Structure and Parameter Learning (World Scientific). His 953 publications include three books; 28 book chapters; 487 journal papers; and 435 refereed conference papers, including about 234 IEEE journal papers in the areas of neural networks, fuzzy systems, brain-computer interface, multimedia information processing, cognitive neuro-engineering, and human-machine teaming, that have been cited more than 45,500 times. Currently, his h-index is 101, and his i10-index is 505.